1 **Tubulinopathy mutations in *TUBA1A* that disrupt neuronal morphogenesis and migration**
2 **override XMAP215/Stu2 regulation of microtubule dynamics**
3

4 Katelyn J. Hoff[1], Jayne E. Aiken[1,2], Mark A. Gutierrez[2], Santos J. Franco[2], Jeffrey K. Moore[1]

5

6 1. Department of Cell and Developmental Biology, University of Colorado Anschutz Medical
7   Campus
8 2. Department of Pediatrics, University of Colorado Anschutz Medical Campus

9

10 **ABSTRACT**

11 Heterozygous, missense mutations in α- or β-tubulin genes are associated with a wide range of

12 human brain malformations, known as tubulinopathies. We seek to understand whether a

13 mutation's impact at the molecular and cellular levels scale with the severity of brain

14 malformation. Here we focus on two mutations at the valine 409 residue of TUBA1A, V409I and

15 V409A, identified in patients with pachygyria or lissencephaly, respectively. We find that ectopic

16 expression of *TUBA1A*-V409I/A mutants disrupt neuronal migration in mice and promote

17 excessive neurite branching and delayed retraction in primary neuronal cultures, accompanied

18 by increased microtubule acetylation. To determine the molecular mechanisms, we modeled the

19 V409I/A mutants in budding yeast and found that they promote intrinsically faster microtubule

20 polymerization rates in cells and in reconstitution experiments with purified tubulin. In addition,

21 V409I/A mutants decrease the recruitment of XMAP215/Stu2 to plus ends and ablate tubulin

22 binding to TOG domains. In each assay tested, the *TUBA1A*-V409I mutant exhibits an

23 intermediate phenotype between wild type and the more severe *TUBA1A*-V409A, reflecting the

24 severity observed in brain malformations. Together, our data support a model in which the

25 V409I/A mutations may limit tubulin conformational states and thereby disrupt microtubule

26 regulation during neuronal morphogenesis and migration.

27

28 **INTRODUCTION**

29 Brain development requires cargo transport, force generation, and structural reinforcement by

30 the microtubule cytoskeleton. The regulation of microtubules must be finely tuned to meet

31 specific demands for different cell types, timepoints in development, and even different locations

32 within a cell. Particularly in neurons, the spatial and temporal regulation of microtubules

33 establishes cargo transport networks, facilitates efficient signal transduction, and supports the

34 extension and retraction of neurites (Dent and Baas, 2014; Dent and Kalil, 2001; He et al., 2002;

35 Lin et al., 2012; Witte et al., 2008). Accordingly, defects in microtubule regulation in neurons

36   have been linked to brain malformations such as lissencephaly, microcephaly, and autism

37   spectrum disorders, among others (Bahi-Buisson et al., 2014; Chakraborti et al., 2016;

38   Srivastava and Schwartz, 2014).

39

40   Brain malformations such as lissencephaly, pachygyria, and polymicrogyria are associated with

41   defects in neuronal migration. During neuronal migration, neurons that are born at the

42   neuroepithelium must migrate out of the ventricular zone along radial glia cells to reach their

43   destination at the cortical plate (Barkovich et al., 2012, 2005). Throughout the course of radial

44   migration cortical neurons must transition through various morphologies, first by transitioning

45   from a bipolar to a multipolar state, then back to a bipolar state to complete migration

46   (Nadarajah et al., 2001; Noctor et al., 2004; Tabata and Nakajima, 2003). After arriving at the

47   cortical plate, the neurons are correctly positioned and polarized to connect to each other and

48   send and receive information. During this dynamic process of neuronal morphogenesis,

49   microtubules generate force and provide structural support during neuronal morphogenesis.

50   Therefore, microtubule networks must be acutely regulated during these transitions (Chesta et

51   al., 2014; Dehmelt et al., 2006; Dent et al., 2011; He et al., 2002; Lu et al., 2013; Sainath and

52   Gallo, 2015; Winding et al., 2016). For example, the microtubule motor, kinesin-6, is important

53   for establishing a leading process that is required for the transition from a multipolar to bipolar

54   state and subsequent neuronal migration (Falnikar et al., 2013). Together this suggests the

55   critical importance of regulating microtubules in the right place and at the right time during the

56   morphological transitions neurons must undergo for migration and, ultimately, proper brain

57   development.

58

59   'Tubulinopathies' encompass a wide range of heterozygous, missense mutations in the genes

60   encoding α- and β-tubulins that are associated with a spectrum of brain malformations.

61   (Bahi-Buisson et al., 2014; Fallet-Bianco et al., 2014). α- and β-tubulins are encoded by a

62   number of different genes, known as isotypes, that differ in amino acid sequence. The

63   expression of different isotypes varies across different cell types as well as during different

64   stages of development. Tubulinopathy mutations have been identified in three of the eight β-

65   tubulin isotypes, and in one of the seven α-tubulin isotypes, a gene known as *TUBA1A* (Bahi-

66   Buisson et al., 2014; Ludueña and Banerjee, 2008). *TUBA1A* is the most highly expressed α-

67   tubulin isotype in post-mitotic neurons in the developing brain (Buscaglia et al., 2020b; Gloster

68   et al., 1994, 1999). To date, a total of 121 heterozygous, missense mutations have been

69   identified in *TUBA1A* and are associated with neurodevelopment disorders (Hebebrand et al.,

70   2019). It remains unclear whether the different severities of malformations observed in these

71   patients are a result of differences in genetic background or are a result of a specific functional

72   difference in the mutant tubulin. A few of these *TUBA1A* mutants have been identified as loss-

73   of-function mutants that are unable to properly assemble into microtubule polymer and thus

74   result in an undersupply of tubulin in the cell (Belvindrah et al., 2017; Keays et al., 2007).

75   However, other *TUBA1A* mutants appear to be gain-of-function, as they are capable of

76   microtubule assembly and act dominantly to perturb microtubule function in migrating neurons

77   (Aiken et al., 2020, 2019). If haploinsufficiency does not explain all *TUBA1A* tubulinopathies,

78   then it is necessary to define clear mechanistic models for how different mutations in α-tubulin

79   can result in different developmental outcomes. Only a small fraction of *TUBA1A* mutants have

80   been studied, and more continued to be identified in the clinic. Therefore, it is important to

81   establish clear mechanistic themes that will be useful in predicting the molecular, cellular, and

82   tissue-level phenotypes of specific mutations.

83

84   The fundamental role of α-tubulin is to complex with β-tubulin into heterodimers and form

85   microtubule polymers that are dynamic and highly regulated via both intrinsic and extrinsic

86   factors (Bodakuntla et al., 2019; Borys et al., 2020; Goodson and Jonasson, 2018; Manka and

87   Moores, 2018; Mitchison and Kirschner, 1984). Purified tubulin assembles into dynamic

88   microtubules in the absence of extrinsic microtubule-associated proteins (MAPs) that are found

89   in cells (Horio and Hotani, 1986; Mitchison and Kirschner, 1984; Walker et al., 1988). This

90   intrinsic activity is in part regulated by the series of conformational states that tubulin undergoes

91   as it transitions from free heterodimer into microtubule polymer (Chrétien et al., 1995;

92   Mandelkow et al., 1991). In recent years, studies using cryo-electron microscopy and

93   recombinant tubulin approaches have advanced the field's understanding of the transitions that

94   accompany GTP hydrolysis as free tubulin assembles into microtubule lattice (Geyer et al.,

95   2018; Manka and Moores, 2018; Roostalu et al., 2020; Zheng et al., 1995). In addition to

96   nucleotide-dependent conformational changes, tubulin must transition from a 'curved' free

97   heterodimer to a straight conformation in the microtubule lattice (Buey et al., 2006; Jánosi et al.,

98   1998; Nawrotek et al., 2011; Nogales and Wang, 2006; Ravelli et al., 2004; Rice et al., 2008).

99   Tubulin domains that control the curved-to-straight transition are not completely understood.

100 The ability of tubulin to adopt a range of conformational states not only impacts its intrinsic

101 microtubule dynamics, but also tubulin's interactions with a wide spectrum of MAPs. For

102 example, doublecortin is predominantly expressed in the developing brain and its N-terminal

103 doublecortin-like (DC) repeat domain binds at the corner of four tubulin subunits in a straight

104   microtubule lattice (Fourniol et al., 2010; Manka and Moores, 2020; Moores et al., 2006). On the
105   other hand, members of the XMAP215 protein family possess a variable number of TOG (tumor
106   overexpressed gene) domains, some of which preferentially bind to curved tubulin (Ayaz et al.,
107   2014, 2012; Slep and Vale, 2007). XMAP215 proteins use this activity to either pull curved
108   tubulin toward the microtubule plus end for polymerization or drive lattice-bound tubulin into a
109   curved state and promote catastrophe (Ayaz et al., 2014; Brouhard et al., 2008; Farmer et al.,
110   2021; Geyer et al., 2018). Therefore, understanding the effects of tubulin conformations on both
111   intrinsic activity and extrinsic regulatory mechanisms are essential for elucidating the regulation
112   of microtubule dynamics.
113
114   In this study we investigate the molecular mechanism of two previously identified tubulinopathy-
115   associated mutations at the valine 409 residue of *TUBA1A*, V409I and V409A. The patient
116   harboring the V409A mutation exhibited lethal lissencephaly, whereas the patient with the V409I
117   mutation presents with a milder malformation known as pachygyria (Bahi-Buisson et al., 2014;
118   Fallet-Bianco et al., 2014). Studying these two mutations that occur at the same residue, yet are
119   associated with varying degrees of brain malformations in patients, has potential to provide
120   insight into how perturbing tubulin activity and the microtubule cytoskeleton in slightly different
121   ways ultimately impacts brain development. We find that the expression of V409I or V409A
122   dominantly disrupts neuron migration in mice *in vivo* and neuron morphologies during *in vitro*
123   development. By modeling the V409I/A mutants at the corresponding residue in budding yeast,
124   V410, we find that the mutants increase microtubule polymerization and depolymerization rates
125   in cells and disrupt the regulation typically conferred by XMAP215/Stu2. We propose that these
126   results are reconciled by the V410I/A mutants adopting a persistently straightened state as
127   compared to WT tubulin, and this drives intrinsically faster microtubule polymerization rates *in*
128   *vitro*. Importantly, we find that the severity of the V409I and V409A mutations scale from protein
129   activity, to microtubule dynamics in cells, to neuron morphology and migration. Our results
130   suggest that the *TUBA1A*-V409I/A mutations cause brain malformations by limiting the
131   conformational transitions of tubulin heterodimers.
132
133   **RESULTS**
134   ***TUBA1A*-V409I/A mutants dominantly disrupt cortical neuron migration**
135   To determine whether *TUBA1A*-V409I/A variants act as loss- or gain-of-function mutations we
136   first sought to establish whether the mutant proteins can polymerize into microtubules. We
137   expressed a hexahistidine (6X-His)-tagged *TUBA1A* construct in cortical neuron cultures

138   harvested from P0 rats. The 6X-His tag was inserted between residues I42 and G43 in a flexible

139   loop of *TUBA1A* that allows for the addition of amino acids without perturbing tubulin function

140   (Buscaglia et al., 2020a). After two days in culture (DIV2) we extracted soluble tubulin from the

141   neurons, fixed the cells, and stained for the 6X-His tag. Both the *TUBA1A*-V409I and -V409A

142   mutants incorporate into microtubules, similar to wild-type (WT) controls, as indicated by the

143   microtubule filaments that can be resolved in the soma (Figure 1A). As a positive control, we

144   expressed the *TUBA1A*-T349E mutant that does not assemble into polymer, as evidenced by

145   the lack of labeled polymer in the soma (Figure 1A). We find that the amount of 6X-His signal

146   retained after soluble protein extraction is similar between WT and V409I/A expressing cells

147   (Figure 1B). These results suggest that the *TUBA1A*-V409I/A mutants assemble into

148   microtubule polymer and have similar levels of microtubule polymer compared to WT.

149

150   We next asked whether incorporation of the *TUBA1A*-V409I/A mutants into microtubules *in vivo*

151   is sufficient to disrupt cortical neuron migration. To answer this question, we performed *in utero*

152   electroporations to ectopically express *TUBA1A* in migrating neurons in the developing mouse

153   brain. At embryonic day (E) 14.5, we electroporated neural progenitors in the cortical ventricular

154   zone, which give rise to immature excitatory neurons that migrate from the ventricular zone into

155   the upper cortical plate. The cDNA expression plasmids used for the electroporations encode

156   for either WT or mutant *TUBA1A*, along with GFP to identify the electroporated cells. The

157   majority of GFP+ neurons ectopically expressing *TUBA1A*-WT successfully migrate from the

158   ventricular zone to the upper cortical plate by E18.5 (Figure 1C). In contrast, neurons ectopically

159   expressing *TUBA1A*-V409I do not migrate to the upper cortical plate as robustly as WT control

160   cells by E18.5, as evidenced by many neurons remaining in the ventricular, subventricular, and

161   intermediate zones. Strikingly, a majority of *TUBA1A*-V409A expressing neurons fail to migrate

162   at all by E18.5 and remain primarily in the ventricular and subventricular zones. To quantify

163   migration for comparison across experiments, we divided the cortical sections into four equal

164   segments from the ventricular zone to the top of the cortical plate and measured the proportion

165   of GFP signal in each segment (Figure 1D). Approximately, the first quartile represents the

166   ventricular and subventricular zones, the second quartile represents the intermediate zone, the

167   third quartile represents the lower cortical plate, and the fourth quartile represents the upper

168   cortical plate. We find that the largest proportion of *TUBA1A*-WT expressing cells (43.4%) are

169   found in the upper cortical plate region (labeled in orange), while the largest proportion of

170   *TUBA1A*-V409I expressing cells (45.4%) are in the intermediate zone and lower cortical plate,

171   and the largest proportion of *TUBA1A*-V409A expressing cells (49.4%) are in the

172   ventricular/subventricular zones (Figure 1E). In each of our experiments, untransfected control

173   cells successfully reach the cortical plate, as evidenced by abundant DAPI signal in the upper

174   cortical plate segment, indicating that the radial glia cells that support migration are not impaired

175   by the transfection of mutant *TUBA1A* in our experiments. These results suggest that the

176   *TUBA1A*-V409I/A mutants act dominantly to disrupt neuron migration, with *TUBA1A*-V409A

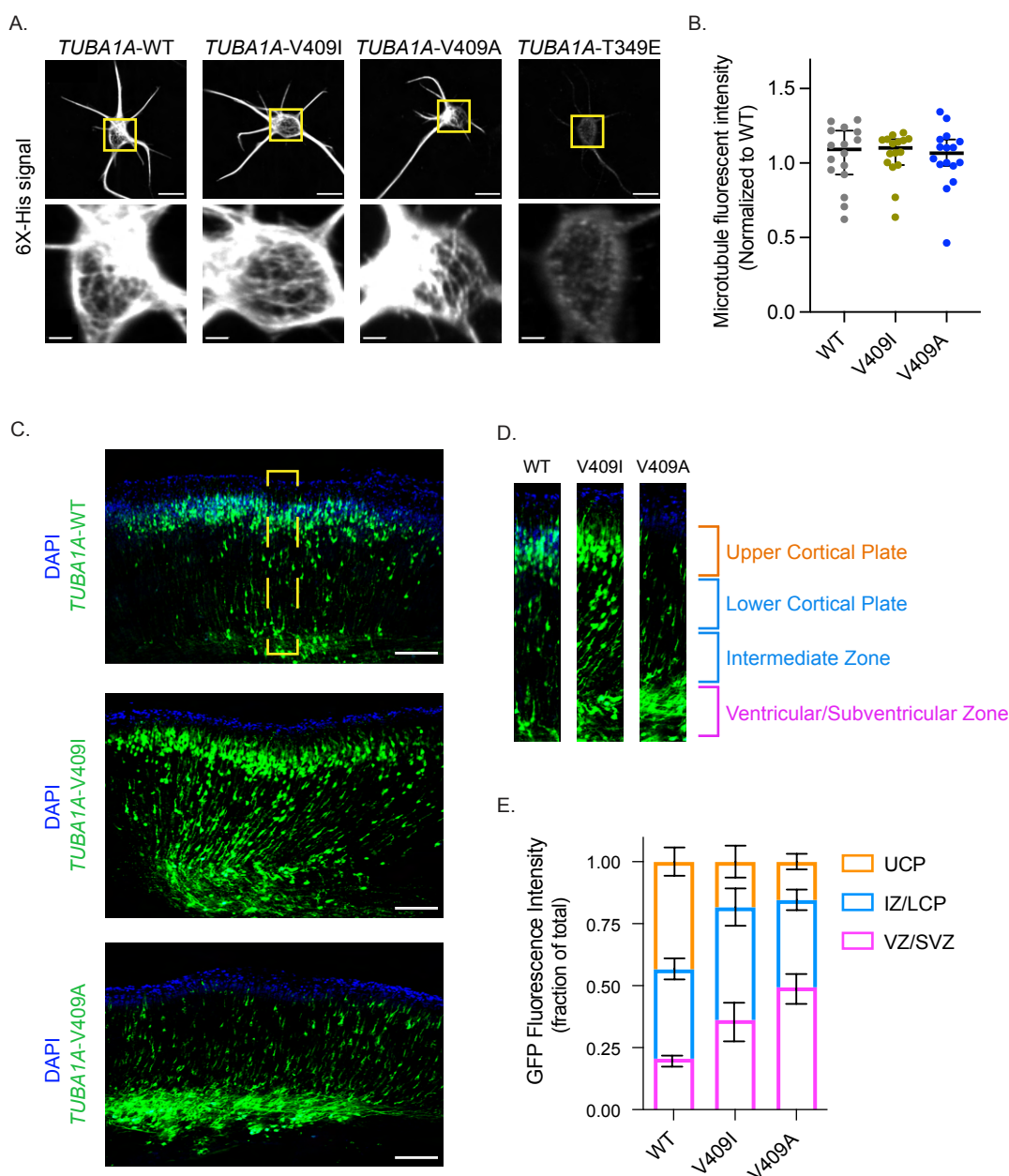177   being more severe than the *TUBA1A*-V409I mutant.

Figure 1.

Figure 1. *TUBA1A*-V409I/A mutants dominantly disrupt cortical neuron migration. A) Representative images of neurons ectopically expressing 6X-His tagged *TUBA1A*-WT, -V409I, -V409A, and -T349E. The soluble tubulin was extracted from the cells, and then cells were stained with an anti-6X-His antibody. Bottom insets are representative of yellow boxes. Scale bar = 10µm in top panels. Scale bar = 2µm in bottom panels. At least 16 neurons were imaged for each condition. **B)** 6X-His fluorescence intensity was measured for each neuron imaged in panel A. Each dot represents a single cell. Bars are median ± 95% confidence interval. **C)** Representative coronal sections of E18.5 mouse brains that were electroporated with the above constructs at E14.5. GFP labels electroporated cells. Scale bar = 200µm. At least 18 brains were imaged for each condition. Yellow box represents region in **(D)**. **(E)** Representative cortical region was divided into 4 equal quartiles and GFP fluorescence intensity was measured in each. 1st quartile = ventricular/subventricular zones (VZ/SVZ), 2nd quartile = intermediate zone (IZ), 3rd quartile = lower cortical plate (LCP), 4th quartile = upper cortical plate (UCP). Bars are mean ± 95% confidence interval.

179   ***TUBA1A*-V409I/A mutants increase neurite branching and delay neurite retraction**

180   The microtubule cytoskeleton plays a crucial role in the series of morphological changes that

181   cortical neurons must undergo throughout the course of radial migration (Nadarajah et al., 2001;

182   Noctor et al., 2004; Tabata and Nakajima, 2003). When immature neurons are born, they

183   extend numerous neurites to probe their environment for directional cues. Once these cues

184   have been identified, neurons must retract most of their neurites and become bipolar, such that

185   one neurite becomes the axon and a neurite on the opposite side of the cell becomes the

186   leading process that guides radial migration. Therefore, it is particularly crucial that microtubules

187   are able to deftly respond to various cues throughout development that promote these different

188   morphology transitions. Therefore, we sought to determine if the *TUBA1A*-V409I/A mutant

189   microtubules perturb neuron morphologies during *in vitro* development. We formed two distinct

190   hypotheses of how *TUBA1A*-V409I/A mutant microtubules could affect neuron morphogenesis:

191   1) insufficient neurite extension, or 2) insufficient neurite retraction.

192

193   To distinguish between these two hypotheses, we first compared the extension of neurites

194   between WT and V409I/A mutants by ectopically expressing the 6X-His-tagged *TUBA1A* (WT or

195   mutant) plasmids described above. We then quantified the number of primary, secondary, and

196   tertiary neurites at two morphologically distinct stages of *in vitro* cortical neuron development,

197   stage 2 (DIV1) and stage 3 (DIV2). Stage 2 neurons are characterized as being multipolar with

198   all neurites being approximately similar in length (Dotti et al., 1988). On average, there is no

199   appreciable difference in the number of neurites quantified in stage 2 cells expressing WT or

200   V409I/A mutant *TUBA1A*. Most neurons at stage 2 have four primary neurites, and we rarely

201   observe secondary or tertiary branches (Supplemental Figure 1A and B). Consistent with this

202   finding, stage 3 WT and V409I/A mutant neurons have a similar number of primary neurites

203   (5.123 ± 0.426, 4.911 ± 0.366, 5.356 ± 0.404 for WT, V409I, and V409A, respectively; Figure 2A

204   and B). However, *TUBA1A*-V409I expressing cells exhibit a slight, but measurable increase in

205   secondary branches as compared to WT cells (0.600 ± 0.227, 0.893 ± 0.264 branches/cell for

206   WT and V409I, respectively; Figure 2B). Strikingly, *TUBA1A*-V409A expressing cells have a

207   significantly greater number of secondary branches, and some also exhibit tertiary branches

208   (Secondary: 0.600 ± 0.227, 2.186 ± 0.682 branches/cell, Tertiary: 0.015 ± 0.031, 0.322 ± 0.171

209   branches/cell for WT and V409A, respectively; Figure 2B). These data fail to support the

210   hypothesis that *TUBA1A*-V409I/A mutants result in insufficient neurite extension because we

211   find a similar number of primary neurites in WT and mutant expressing cells. Our data instead

8

212   lend support to the alternative hypothesis that there is insufficient neurite retraction, as

213   evidenced by the increase in neurite branching.

214

215   To address this, we tested whether the neuron microtubules respond to destabilizing cues that

216   are necessary for neurite retraction. We stimulated neurite retraction *in vitro* by placing the

217   neuron cultures at 4˚C over the course of six hours. At low temperatures, microtubules

218   destabilize, which ultimately leads to neurite retraction (Breton and Brown, 1998; Tilney and

219   Porter, 1967; Weber et al., 1975). During our time course experiment, samples from each

220   genotype were fixed at two-hour intervals and stained for β-II tubulin, a highly abundant β-

221   tubulin isotype in cortical neurons, to label microtubules in neurites. After two hours at 4˚C,

222   *TUBA1A*-WT expressing cells (identified by cytoplasmic GFP) lost most neurites, and those that

223   remain formed the retraction bulbs that are characteristic of retracting neurites (Figure 2C and

224   Supplemental Figure 1C). By four and six hours of cold exposure, β-II tubulin signal is only

225   found in the cell soma of neurons expressing *TUBA1A*-WT. In contrast, most *TUBA1A*-V409I

226   expressing cells do not exhibit retraction bulbs or neurite loss until four hours of 4˚C exposure.

227   The most severe defect is detected in *TUBA1A*-V409A expressing cells where neurites are

228   maintained throughout most of the time course, with retraction bulbs beginning to form only after

229   six hours of the 4˚C exposure. Together, these data suggest that expression of *TUBA1A*-V409I

230   or -V409A creates hyper-stable neurites and, particularly in the case of V409A, excessive
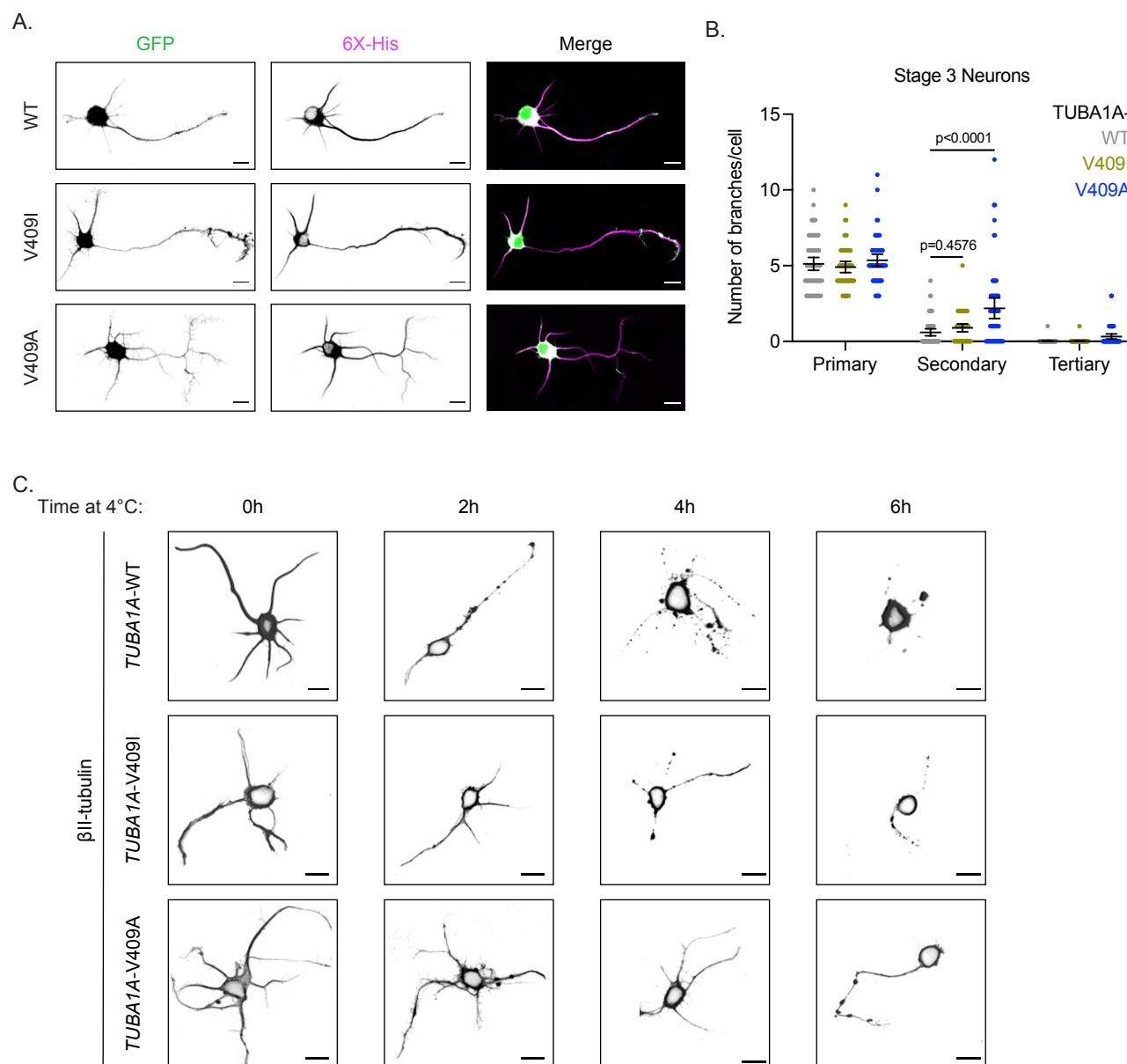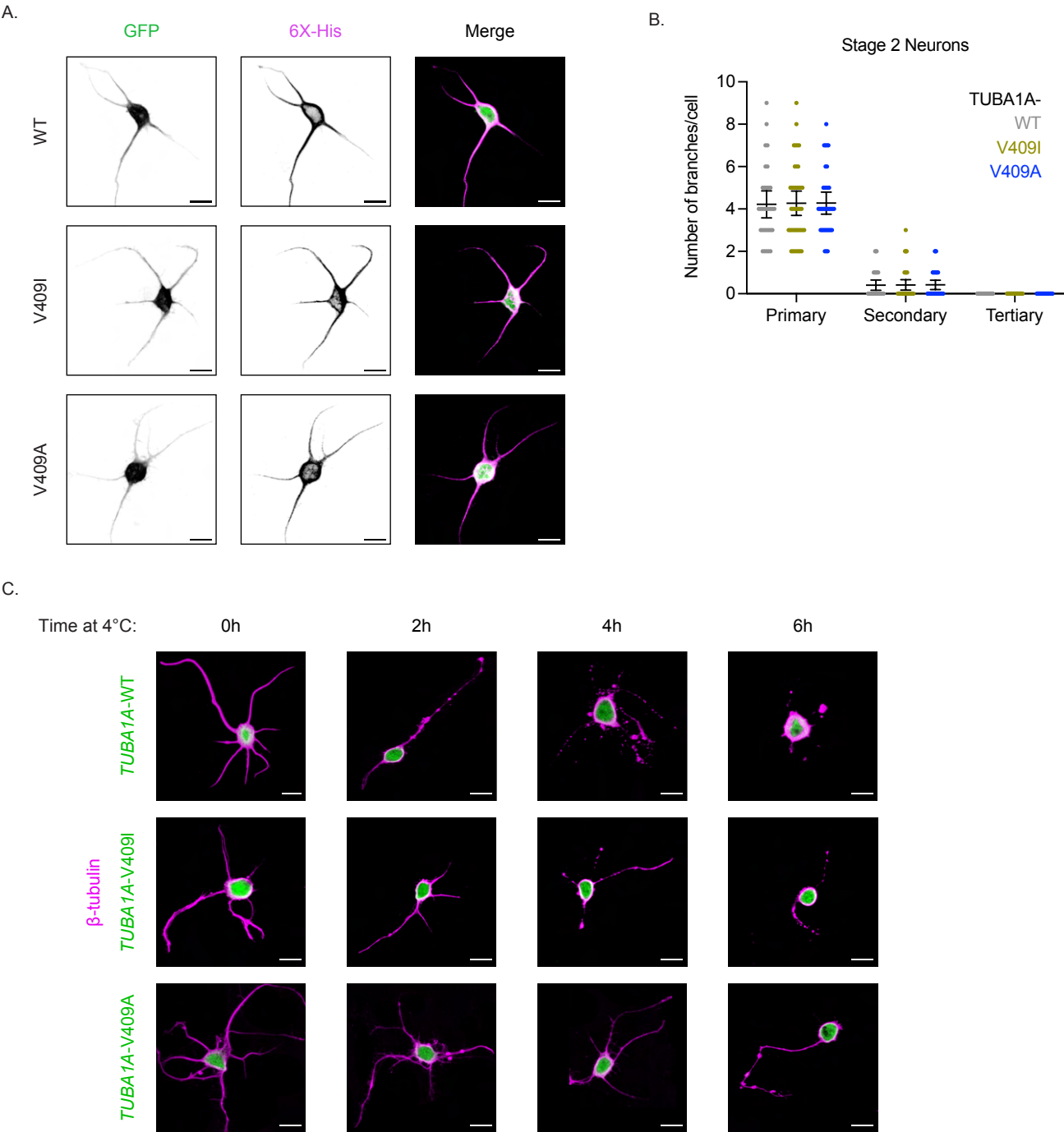
231   neurite branching.

Figure 2.

Figure 2. *TUBA1A*-**V409I/A mutants alter neuron morphologies. A)** Representative DIV2 cortical neurons expressing cytoplasmic GFP and 6X-His tagged *TUBA1A*-WT, -V409I, and -V409A. Scale bar = 10μm. At least 27 neurons were imaged for each condition. **B)** Quantification of number of primary, secondary, and tertiary branches in each condition. Each dot represents a single cell. Bars are mean ± 95% confidence interval. **C)** Representative images of neurons expressing the above plasmids, exposed to 4°C for indicated time, and stained with TUBB2A/B. Scale bar = 10μm.

Supplemental Figure 1.

Supplemental Figure 1. Effect of *TUBA1A*-V409I/A on neuronal morphologies. A) Representative DIV1 cortical neurons expressing GFP and 6X-His tagged *TUBA1A*-WT, -V409I, and -V409A. Scale bar = 10μm. At least 23 neurons were imaged for each condition. **B)** Quantification of number of primary, secondary, and tertiary branches in each condition. Each dot represents a single cell. Bars are mean ± 95% confidence interval. **C)** Representative merge images of neurons expressing the above plasmids, exposed to 4°C for indicated time, stained with TUBB2A/B in magenta, and expressing cytoplasmic GFP in green. Scale bar = 10μm.
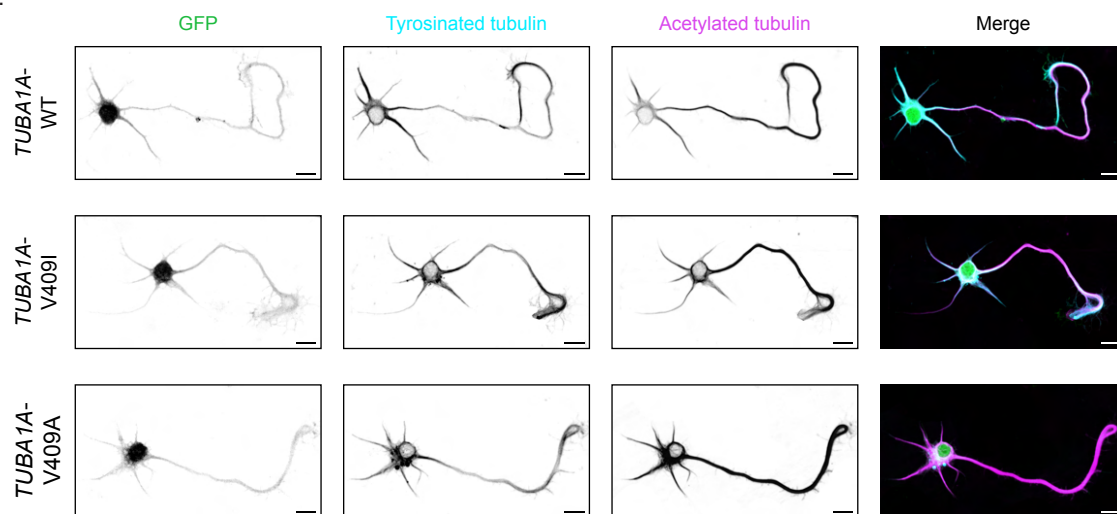
234 **_TUBA1A_-V409I/A mutant microtubules have high levels of acetylation**

235 We next sought to determine if the increase in neurite branching and resistance to cold-induced

236 neurite retraction seen in _TUBA1A_-V409I/A expressing cells is a result of altered microtubule

237 dynamics. To test this, we quantified levels of tubulin post-translational modifications in WT- and

238 mutant-expressing cells. Tyrosinated tubulin is a marker of dynamic, newly formed microtubules

239 and is typically evenly distributed amongst the axon and dendrites (reviewed in Westermann

240 and Weber, 2003). Acetylated tubulin is a marker of stable microtubules and is highly localized

241 to the axon, but largely absent in the dendrites.

242

243 As expected, stage 3 control cells ectopically expressing _TUBA1A_-WT have acetylated tubulin

244 localized to the axon and tyrosinated tubulin throughout the neuron (Figure 3A and B). Both

245 _TUBA1A_-V409I and -V409A expressing neurons also exhibit tyrosinated tubulin throughout the

246 neuron, similar to that observed in control cells expressing _TUBA1A_-WT (Axons: 0.487 ± 0.061,

247 0.507 ± 0.069, 0.471 ± 0.070A.U. and Dendrites: 0.524 ± 0.069, 0.511 ± 0.072, $0.543 \pm$

248 0.083A.U. for WT, V409I, and V409A, respectively; Figure 3A and B). _TUBA1A_-V409I

249 expressing cells have a modest increase in acetylated tubulin in both the axon and dendrites,

250 and _TUBA1A_-V409A expressing cells exhibit a striking increase in microtubule acetylation in all

251 neurites and even in the soma (Axons: 2.861 ± 0.227, 3.025 ± 0.253, 3.721 ± 0.295A.U. and

252 Dendrites: 1.239 ± 0.204, 1.492 ± 0.145, 2.395 ± 0.184A.U. for WT, V409I, and V409A,

253 respectively; Figure 3A and C). Although acetylated tubulin levels are increased in the _TUBA1A_-

254 V409I/A mutants, our experiments where soluble tubulin is extracted indicate that the total

255 amount of microtubule polymer is similar between WT and mutant-expressing cells (Figure 1B).

256 This suggests that increased microtubule acetylation in cells expressing V409I/A mutants is not

257 simply attributable to increased microtubule polymer, but rather increased levels of acetylation
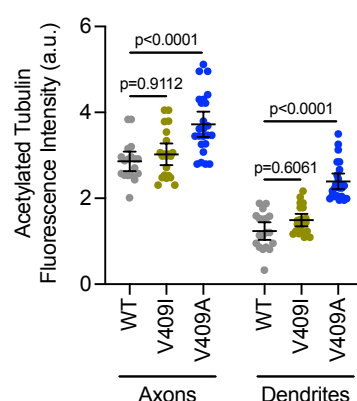
258 on the microtubules.

Figure 3.
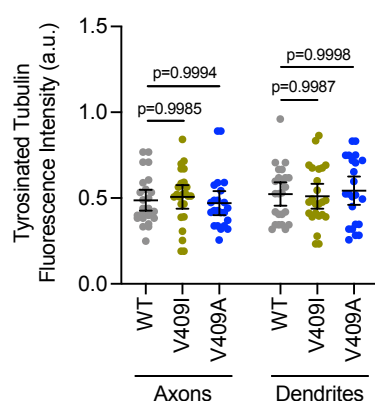
Figure 3. *TUBA1A*-V409I/A microtubules have increased acetylation levels. A) Representative DIV2 cortical neurons expressing plasmids with cytoplasmic GFP and 6X-His tagged *TUBA1A*-WT, -V409I, and -V409A. Cells stained with tyrosinated tubulin and acetylated tubulin. Scalebar = 10µm. Quantification of tyrosinated tubulin **(B)** and acetylated tubulin **(C)** fluorescence intensity in a cell's axon and dendrites. Each dot represents quantification of a single cell. Bars are mean ± 95% confidence interval.

Modeling *TUBA1A*-V409I/A mutants in budding yeast reveals altered microtubule dynamics

The α-tubulin V409 residue is highly conserved across eukaryotes (Figure 4A). To better understand the molecular impact of the *TUBA1A*-V409I/A mutants, we created analogous mutants at the corresponding residue in *Saccharomyces cerevisiae* (or budding yeast), V410. Using this system, we created strains in which all the α-tubulin expressed in the cell was either WT, V410I, or V410A. We find that compared to WT, V410I cells have no significant change in fitness, while V410A cells exhibit a slight fitness defect, as indicated by a 4.4% increase in doubling time (Supplemental Figure 2A). By introducing either the V410I or V410A mutation into both α-tubulin isotypes of budding yeast (*TUB1* and *TUB3*), we can measure the dynamics of individual microtubules that consist of a homogenous supply of either WT or mutant α-tubulin. Thus, any effect we see on dynamics would be a result of the mutant of interest as opposed to a compensatory response by alternative tubulin isotypes.

To track the length of individual microtubules over time in cells, we used Bik1-3GFP, the yeast homologue of CLIP-170, as a marker for microtubule plus-ends (Figure 4B and 4C). Compared to WT, we find that *tub1*/*tub3*-V410A mutant microtubules have significantly faster polymerization rates, while *tub1*/*tub3*-V410I microtubules have intermediate rates between WT and V410A mutants (1.078 ± 0.078, 1.463 ± 0.112, 1.625 ± 0.117µm/min for WT, V410I, and V410A, respectively; Figure 4D). Similarly, *tub1*/*tub3*-V410A microtubules, and to a lesser extent -V410I microtubules, have faster depolymerization rates compared to WT (1.861 ± 0.165, 2.300 ± 0.166, 2.788 ± 0.256µm/min for WT, V410I, V410A, respectively; Figure 4E). Our data also shows that *tub1*/*tub3*-V410A microtubules exhibit very few catastrophes compared to WT, and the *tub1*/*tub3*-V410I microtubules again have an intermediate catastrophe frequency (1.216 ± 0.105, 0.973 ± 0.111, 0.761 ± 0.106 events/minute for WT, V410I, and V410A, respectively; Figure 4F). Accordingly, *tub1*/*tub3*-V410A mutant microtubules reach longer median lengths than either the *tub1*/*tub3*-V410I or WT microtubules (0.66, 0.68, 0.90µm for WT, V410I, V410A, respectively; Figure 4G). Additionally, we find that astral microtubules in *tub1/tub3*-V410A mutant cells are retained for a longer time at 4°C than those in WT control cells, and *tub1/tub3*-V410I microtubules have an intermediate phenotype (Figure 4H). Summarizing these dynamics data, we find that α-tubulin-V410I/A microtubules, and particularly the *tub1*/*tub3*-V410A variant, exhibit faster microtubule polymerization rates and decrease how often the microtubule

292   catastrophes. However, when these mutant microtubules do catastrophe, they depolymerize at

293   a faster rate than WT.

294

295   To understand how the different microtubule parameters described above work together to

296   influence microtubule activity, we calculated the dynamicity of WT and *tub1*/*tub3*-V410I/A

297   microtubules. Dynamicity is defined as the total change in microtubule length divided by the

298   change in time (Jordan et al., 1993). We find that *tub1*/*tub3*-V410A microtubules have the

299   highest dynamicity values, while *tub1*/*tub3*-V410I microtubules have an intermediate dynamicity

300   between -V410A and WT (0.443 ± 0.028, 0.507 ± 0.034, 0.563 ± 0.047 subunits/second; Figure

301   4I). Similar to our work in neurons, the V410A mutant has the strongest effect on microtubule

302   dynamics while the V410I mutant has a more intermediate impact. Together, the results of

303   modeling these patient-associated mutations in budding yeast indicates that the α-tubulin-

304   V410I/A mutations are sufficient to alter microtubule dynamics in this system.

Figure 4.

Figure 4. Modeling _TUBA1A_-V409I/A mutants in budding yeast reveals altered microtubule dynamics. A) Sequence alignment of human, mouse, and rat TUBA1A and budding yeast α-tubulins Tub1 and Tub3. Valine 409 is highlighted in yellow and resides in a highly conserved helix known as H11'. **B)** Representative image of budding yeast cell with microtubule plus-end binding protein Bik1 labeled with 3GFP. Scalebar = 1μm. **C)** Life plot of the dynamics of individual microtubules from WT (gray) and V410A (blue) cells showing the change in length over time. **D)** Polymerization rates of astral microtubules. Each dot represents a single polymerization event. Bars are mean ± 95% confidence interval. **E)** Depolymerization rates of astral microtubules. Each dot represents a single depolymerization event. **F)** Catastrophe frequency for astral microtubules expressed as the number of catastrophe events that occur per minute. Each dot represents the average catastrophe frequency of a single cell. **G)** Histogram of all astral microtubule lengths from time lapse imaging of WT, V410I, and V410A cells. **H)** Proportion of cells with astral microtubules after indicated time at 4°C. Symbols represent average of 3 independent experiments where at least 295 cells were analyzed per condition. **I)** Dynamicity of astral microtubules calculated as the total change in length divided by the total change in time. Each dot represents the calculated dynamicity value of a single cell. For all measured dynamics, at least 28 cells were measured for each genotype.

Supplemental Figure 2.

A.
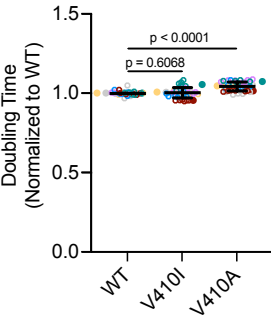
Supplemental Figure 2. Fitness assay for V410I/A yeast mutants. A) Doubling times of cells expressing the indicated mutation at the genomic *TUB1* locus. 6 samples containing 2 different isolates for each strain were tested in 3 independent experiments. Bars are mean ± 95% confidence interval.

307 ***tub1/tub3*-V410I/A microtubules have decreased localization of and affinity for**

308 **XMAP215/Stu2**

309 Microtubule dynamics in cells are the product of both intrinsic tubulin activity, as well as

310 regulation by extrinsic MAPs. Therefore, we sought to determine how *tub1/tub3*-V410I/A affect

311 extrinsic and/or intrinsic modes of regulation to alter microtubule dynamics. The α-tubulin V409

312 (human) or analogous V410 (yeast) residue resides on the external surface of the tubulin

313 heterodimer near the binding sites of a wide variety of microtubule-associated proteins (Löwe et

314 al., 2001). In particular, one structural analysis highlights the α-tubulin V410 residue as a

315 potential interactor with the TOG2 domain of Crescerin1 (Das et al., 2015). The Crescerin1

316 TOG2 domain has a similar structure to the TOG1 domain of Stu2, the yeast homologue of

317 XMAP215. As Stu2/XMAP215 is the major microtubule polymerase in cells, we predicted that

318 the increase in microtubule polymerization observed in *tub1/tub3*-V410I/A cells could be a result

319 of increased Stu2 activity on the mutant microtubules. To test this, we first used Stu2-3GFP to

320 measure Stu2 localization at astral microtubule plus ends in cells where all the α-tubulin is either

321 WT, V410I, or V410A mutant (Figure 5A). We find that *tub1/tub3*-V410A mutant microtubules

322 have significantly decreased Stu2-3GFP fluorescence intensity at the plus ends compared to

323 WT, while *tub1/tub3*-V410I microtubules have an intermediate phenotype between the two

324 (3203 ± 333, 1860 ± 165, 1365 ± 143A.U. for WT, V410I, and V410A, respectively; Figure 5B).

325 Thus, despite having increased microtubule polymerization rates, the *tub1/tub3*-V410I/A mutant

326 microtubules have less Stu2 at microtubule plus ends.

327

328 Stu2 is comprised of two TOG domains (TOG1 and TOG2) that bind specifically to free tubulin

329 heterodimer and are necessary for concentrating tubulin at microtubule plus ends to promote

330 microtubule polymerization. Disrupting the interaction between the Stu2 TOG2 domain and

331 tubulin heterodimers decreases the localization of Stu2 to microtubule plus ends (Geyer et al.,

332 2018). We therefore predicted that the decreased localization of Stu2 at *tub1/tub3*-V410I/A

333 microtubule plus ends may be a result of lowered affinity between the mutant tubulins and Stu2

334 TOG domains. To test this prediction, we purified tubulin heterodimer from budding yeast in

335 which the purified α-tubulin was either Tub1-WT, -V410I, or -V410A. Additionally, we purified the

336 two TOG domains in Stu2 fused to a GST tag (referred to as GST-TOG1/2). Using a low

337 concentration of either WT or V410I/A mutant tubulin in the presence of increasing

338 concentrations of GST-TOG1/2, we find that V410I, and more significantly V410A, mutant

339 tubulin has decreased affinity for GST-TOG1/2 as compared to WT (Figure 5C and

340 Supplemental Figure 3A). For reference we used previously published K_D values for WT yeast

18

341   tubulin affinity for either TOG1 or TOG2 to determine an expected binding curve (Geyer et al.,

342   2015). These results indicate that the decrease in Stu2 localization we see at the *tub1/tub3*-

343   V410I/A microtubule plus ends is a consequence of the decreased affinity of Stu2 TOG1/2

344   domains for the mutant tubulin.

345

346   Stu2 is an essential gene in budding yeast, presumably because of its important role in

347   regulating microtubule dynamics (Wang and Huffaker, 1997). Based on the increased

348   microtubule polymerization rates observed for V410I/A microtubules, and the decreased affinity

349   between V410I/A and Stu2 TOG domains, we predicted that *tub1/tub3*-V410I/A microtubules

350   would be resistant to the depletion of Stu2. To test this, we constructed *tub1*-V410I or -V410A

351   yeast strains where we could conditionally deplete Stu2 (Kosco et al., 2001). Upon addition of

352   copper to the media of these cells, synthesis of *STU2* mRNA is repressed and Stu2 is

353   degraded. We find that after 1.5 hours in 500µM copper sulfate ($CuSO_4$), Stu2-HA is almost

354   undetectable via western blot (Figure 5D and Supplemental Figure 3B). Under these conditions,

355   the proportion of WT cells with visible astral microtubules decreases from 53% to 34% (0.526 $\pm$

356   0.036, 0.345 $\pm$ 0.27 at 0 and 1.5 hours, respectively; Figure 5E-F). In contrast, *tub1*-V410I and

357   *tub1*-V410A cells have no significant decrease in proportion of cells that have astral

358   microtubules after 1.5 hours of Stu2 depletion (V410I: 0.537 $\pm$ 0.023, 0.516 $\pm$ 0.022, V410A:

359   0.524 $\pm$ 0.036, 0.588 $\pm$ 0.011 at 0 and 1.5 hours, respectively; Figure 5E-F). These data indicate

360   that V410I and V410A microtubules persist in the absence of Stu2, and therefore the mutant

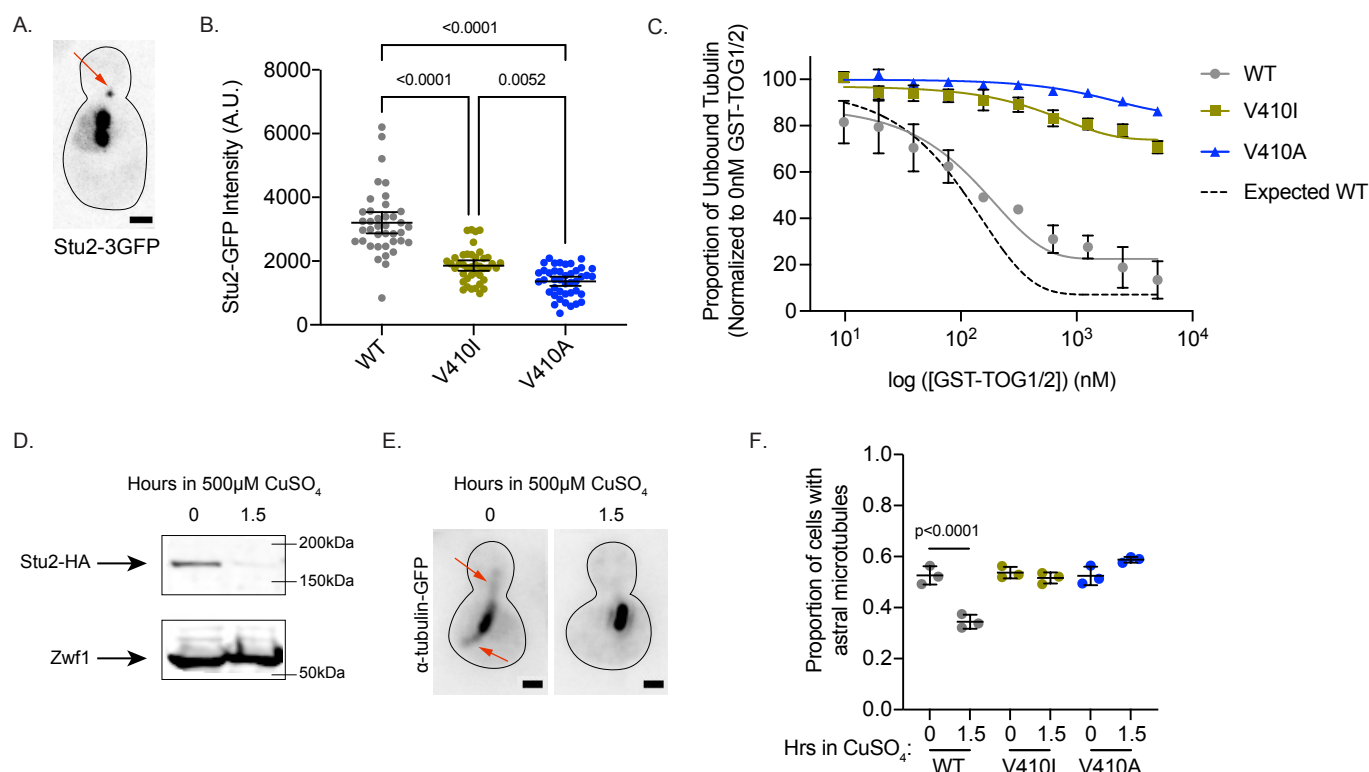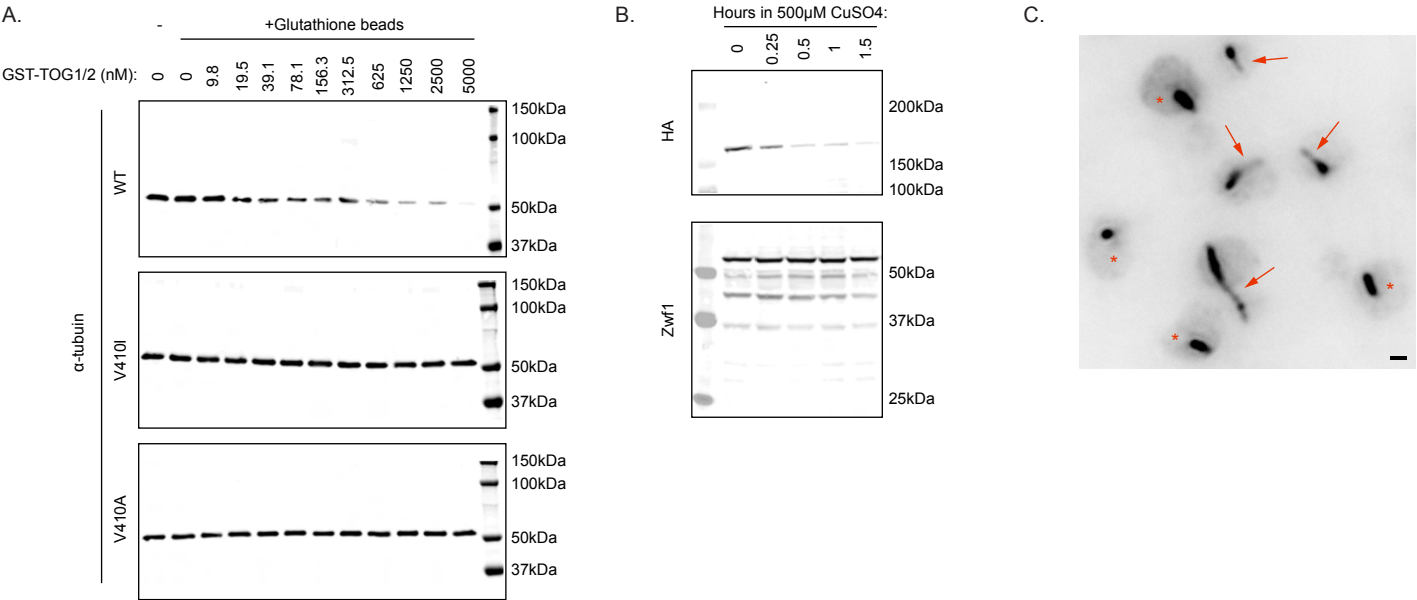361   tubulins may not require Stu2 polymerase activity to the same extent as WT.

Figure 5.

Figure 5. V410I/A mutants subvert Stu2 regulation. A) Representative image of budding yeast cell expressing Stu2-3GFP. Red arrow indicates Stu2 at microtubule plus end. Scale bar = 1µm. **B)** Quantification of Stu2-3GFP fluorescence intensity at microtubule plus ends. Each dot represents the quantification from a single cell. Bars are mean ± 95% confidence interval. At least 39 cells were analyzed per condition. **C)** Proportion of unbound tubulin in solution in the presence of increasing concentrations of GST-TOG1/2. Data was analyzed from the α-tubulin signal on supernatant samples run on western blots. Each condition was normalized to the constant amount of tubulin added to each sample in the absence of GST-TOG1/2. Dots represent averages from three separate experiments. Bars are standard error of the mean. **D)** Western blot of protein lysate from cells induced with 500µM $CuSO_4$ for 0 and 1.5 hours. Blots were probed for HA and Zwf1. **E)** Example images of WT cells induced with 500µM $CuSO_4$ for 0 and 1.5 hours stained for α-tubulin. Red arrows indicate astral microtubules. Scale bar = 1µm. **F)** Quantification of proportion of cells imaged that have at least one astral microtubule. Each dot represents the average proportion of cells from three separate experiments. At least 800 cells were measured for each condition. Bars are mean ± standard error of the mean.

bioRxiv preprint doi: https://doi.org/10.1101/2021.12.06.471490; this version posted December 7, 2021. The copyright holder for this preprint (which was not certified by peer review) is the author/funder. All rights reserved. No reuse allowed without permission.

Supplemental Figure 3.

Supplemental Figure 3. V410I/A mutants affect Stu2 interactions and regulation. A) Representative western blots of WT, V410I, and V410A samples probed for α-tubulin in the absence of glutathione beads, as well as in the presence of glutathione beads and increasing concentrations of GST-TOG1/2. **B)** Representative western blot of WT cells induced with 500µM $CuSO_4$ for indicated number of hours. Blots were probed with HA and Zwf1 antibodies. **C)** Large field representative image of WT cells in the absence of 500µM $CuSO_4$ stained for α-tubulin. Red arrows represent cells with at least one astral microtubule. Red stars represent cells without an astral microtubule. Scale bar = 1µm.

365 **Purified *tub1*-V410A has increased microtubule polymerization rates *in vitro***

366 Stu2 TOG domains preferentially bind to the kinked conformation of tubulin and have low affinity

367 for straight heterodimers (Ayaz et al., 2014, 2012). Based on our *in vitro* binding assays, we

368 hypothesized that α-tubulin V410I/A pushes the heterodimer into a straightened state. The V410

369 residue resides in helix 11' of α-tubulin, which is located at the hinge point between α- and β-

370 tubulin (Löwe et al., 2001), and makes it a prime candidate for affecting the conformational

371 states of the heterodimer. We predicted that a straighter heterodimer would increase

372 microtubule polymerization rates as a straight heterodimer is more compatible with forming the

373 microtubule lattice. Therefore, we reasoned that if the changes observed in V410I/A microtubule

374 dynamics are a result of a straightened heterodimer conformation, the mutants should have

375 intrinsically faster polymerization rates *in vitro*.

376

377 To test this, we used interference reflection microscopy (IRM) to measure the intrinsic

378 polymerization activity of our purified yeast Tub1-WT, -V410I, and -V410A heterodimers in an *in*

379 *vitro* dynamics assay. We used GMPCPP-stabilized, rhodamine-labeled porcine microtubule

380 'seeds' attached to the surface of the coverslip via anti-rhodamine antibodies to nucleate the

381 assembly of microtubules from the purified tubulin in the reaction (Figure 6A). We used three

382 concentrations of purified tubulin, between 0.5 and 0.9μM, to measure microtubule dynamics *in*

383 *vitro*. Within this concentration range, we find that soluble tubulin assembles from the stabilized

384 seeds and forms dynamic microtubules. If tubulin concentration is too high, the tubulin will

385 spontaneously nucleate away from the stabilized seeds (to form microtubules, oligomers,

386 aggregates, etc.) and will not be visible on the microscope. If the tubulin concentration is too

387 low, the tubulin will not sustain assembly from the seeds. In our experimental set up, we are

388 unable to observe microtubule dynamics below 0.5μM tubulin. For each concentration, we

389 measured the change in microtubule length over time of WT or V410I/A mutant tubulin in a

390 completely purified system using unlabeled tubulin (Figure 6B, Supplemental Video 1).

391

392 In contrast to our results in budding yeast cells, we find that purified tub1-V410I microtubules do

393 not have significantly increased polymerization rates as compared to WT at any of the three

394 concentrations tested (Figure 6C). However, with purified tub1-V410A tubulin, we were unable

395 to observe microtubule dynamics at these three concentrations, nor did we observe any at

396 higher concentrations up to 1.5μM or lower concentrations down to 0.1μM (data not shown).

397 Based on our previous data, we predict that tub1-V410A tubulin exhibits increased assembly

398 activity and would be more dynamic at lower concentrations. If tub1-V410A tubulin exhibits

22

399   higher assembly activity than WT tubulin, even the low end of our usable concentration range

400   may be too high for this mutant, and we would be unable to visualize microtubule dynamics

401   because the mutant may readily assemble away from seeds (similar to top panel of Figure 6A).

402   To circumvent these issues while still testing the intrinsic capabilities of tub1-V410A, we mixed

403   WT and tub1-V410A tubulin in a one-to-one ratio, for a total tubulin concentration of 0.5, 0.7, or

404   0.9μM. At this WT:V410A one-to-one ratio, we find an increase in microtubule polymerization

405   rates at each concentration tested (Figure 6C). Since the amount of either WT or V410A tubulin

406   that is present in each of these one-to-one mixtures (i.e., 0.25, 0.35, or 0.45μM) is not sufficient

407   to support microtubule assembly on its own, we conclude that the increased microtubule

408   polymerization is a synergistic effect of the blend of WT and V410A mutant tubulin.

409

410   The fitted lines of the data collected at each tubulin concentration provide us with important

411   information about the intrinsic properties of the WT and mutant microtubules formed *in vitro*. The

412   slopes of the fitted lines represent the concentration-dependent polymerization rate, and we find

413   that WT/V410A has a ~2-fold increased rate as compared to WT and V410I (11.6 compared to

414   5.8 and 6.5μm/hr/μM). The x- and y-intercepts represent the critical concentration and apparent

415   off rate constants, respectively (x-intercepts = 0.01, 0.02, and 0.02μM; y-intercepts = -0.07, -

416   0.13, and -0.18μm/hr for WT, V410I, and WT/V410A, respectively). In contrast to the increase

417   observed in microtubule polymerization rates, the microtubule depolymerization rates were not

418   different between WT and either the V410I or V410A mutants (Figure 6D). These data indicate

419   that *tub1*-V410A has significantly increased intrinsic microtubule polymerization as compared to

420   WT. Together, our data explain the intrinsic mechanism by which the V409/V410A mutant has

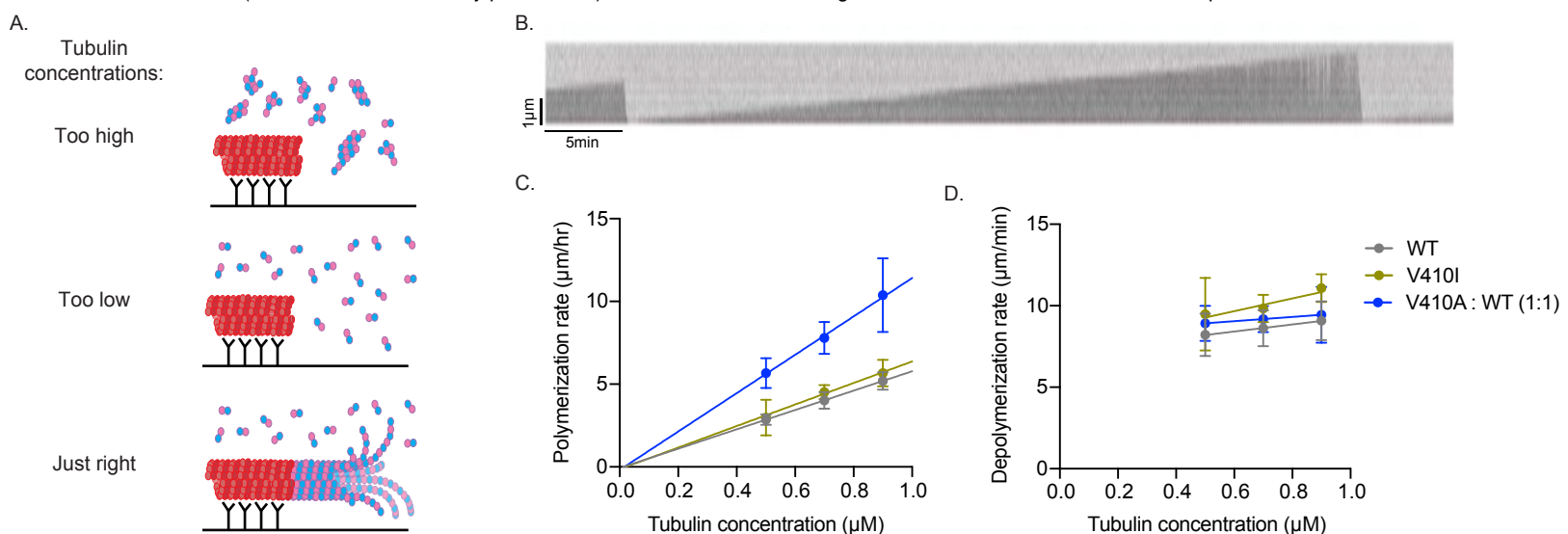421   the most severe phenotypes across scales, while V409/V410I has more mild effects.

Figure 6. V410A has intrinsically faster microtubule polymerization rates *in vitro*. A) Graphic depicting aggregates and non-seeded nucleation when tubulin concentrations are too high, no nucleation when concentrations are too low, and dynamic microtubules when concentrations are at an appropriate level. **B)** Example kymograph of dynamic microtubule from purified budding yeast tubulin measured using interference reflection microscopy. X and Y scale bars = 5 minutes and 1μm, respectively. **C)** Microtubule polymerization rates at 0.5, 0.7, and 0.9μM of tubulin. Each data point represents the mean of three independent experiments in which at least 28 dynamic microtubules were measured per condition. Error bars are mean ± 95% confidence interval. **D)** Microtubule depolymerization rates.

Figure 7.
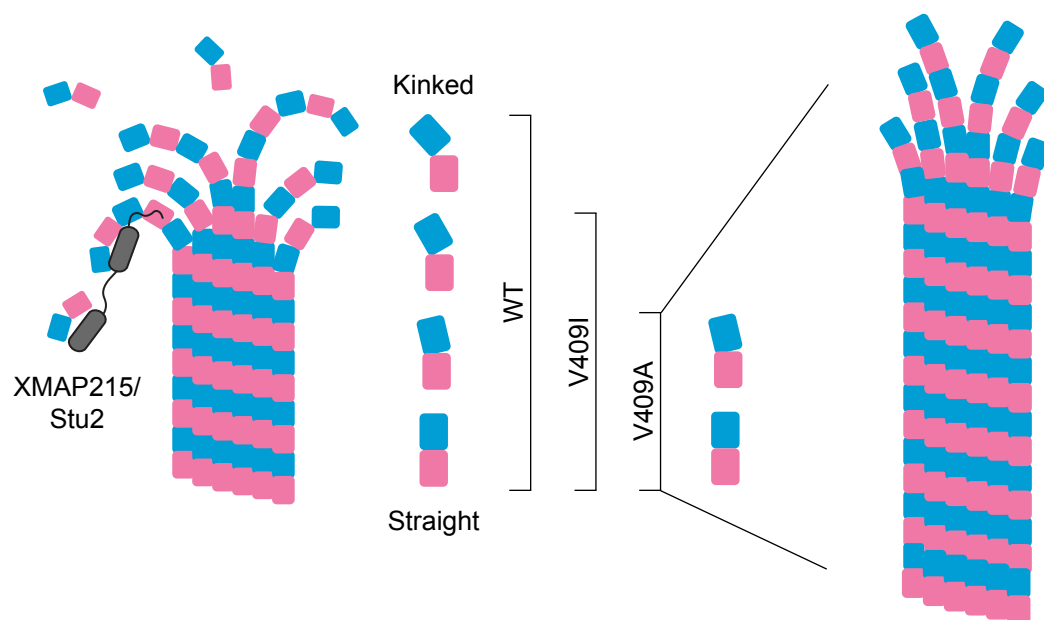
Figure 7. Proposed model for α-tubulin V409I and V409A on tubulin conformations and microtubule assembly. WT tubulin undergoes a series of conformational states as it transitions from a curved free heterodimer into the straight microtubule lattice. Our data support a model in which V409I, and more severely V409A, limit the range of conformations the heterodimer can adopt and push the heterodimer into a straightened state. Additionally, these mutants result in longer-lived microtubules that polymerize faster. We propose that this is due in part to the straighter mutant tubulin being more compatible with assembling into the microtubule lattice, as well as the mutants subverting normal XMAP215/Stu2 regulation.

DISCUSSION

The missense, heterozygous mutations identified in human tubulin genes and associated with brain malformations are numerous and varied (Bahi-Buisson et al., 2014; Fallet-Bianco et al., 2014). To date, we do not have a good understanding of how different mutations in tubulin genes have such a wide spectrum of detrimental effects on brain development. Investigating the molecular impact of different tubulinopathy mutations and how these mutants affect greater tissue level development is critical to advancing our understanding of the role of the microtubule cytoskeleton during neurodevelopment and disease. In this study, we aim to determine the mechanism of two different substitutions at the valine 409 residue of *TUBA1A* that are associated with different severities of brain malformations. We find that ectopically expressed *TUBA1A*-V409I/A mutants assemble into microtubules in neuron cultures and dominantly disrupt radial neuron migration, and most significantly in cells expressing *TUBA1A*-V409A (Figure 1). Our work indicates that the mutation associated with the most severe brain phenotype, *TUBA1A*-V409A, also has the most severe impact on neurite branching and microtubule dynamics, while the milder -V409I mutant has intermediate phenotypes. These findings provide evidence that the impact of tubulinopathy mutations scale up from altered microtubule polymerization activity and loss of regulation by microtubule-associated proteins to cellular and tissue defects.

As neurons migrate from the ventricular zone to the cortical plate, they must transition through different polarization states (Nadarajah et al., 2001; Noctor et al., 2004; Tabata and Nakajima, 2003). The overexpression or depletion of a wide variety of signaling molecules and cytoskeletal proteins delay or inhibit neuron morphology transitions that impair subsequent migration (reviewed in Cooper, 2014). Several cases of brain malformations similar to those investigated in this study have been linked to mutations that disrupt radial migration by inhibiting the multipolar-to-bipolar transition (e.g., loss-of-function Cdk5 mutations; Ohshima et al., 2007). While there are numerous factors that are required for proper neuron migration, our data support a hypothesis that *TUBA1A*-V409I/A mutants disrupt and/or delay proper morphology transitions. At the cellular level, we find that neurons ectopically expressing *TUBA1A*-V409I and -V409A disrupt neuron morphogenesis by promoting excessive branch stabilization (Figure 2A and B). Additionally, neurons expressing *TUBA1A*-V409I/A are more resistant to cold temperature-induced neurite retraction as compared to cells solely expressing WT tubulin (Figure 2C). To the best of our knowledge, there are no tubulinopathy mutations to date that disrupt neuron migration via impaired neuron morphology transitions. Therefore, future work will

26

458   be required to determine whether this is a common mechanism for particular types of brain

459   malformations.

460

461   Our findings support the idea that microtubule stability plays a determining role in neuron

462   branching and morphogenesis. Previous studies have identified that taxol-treated neurons have

463   an increase in neurite extension, axon formation, and branching, while nocodazole treatments

464   result in diminished neurite extension and increased retraction (He et al., 2002; Witte et al.,

465   2008). The altered expression of, or mutations in, microtubule-associated proteins also alter

466   neuron morphogenesis (reviewed in Lasser et al., 2018). For example, the microtubule-

467   associated protein SSNA1 also promotes axonal branching by mediating microtubule nucleation

468   and branching, further highlighting the role of microtubule dynamics play in neuron

469   morphogenesis (Basnet et al., 2018). Neurons must tightly control both microtubule turnover

470   and nucleation to control neurite branching (Basnet et al., 2018; Witte et al., 2008). Both taxol-

471   treatment and SSNA1 overexpression result in increased neurite branching, yet each drive this

472   phenotype via separate mechanisms; Taxol suppresses microtubule turnover, whereas

473   overexpression of SSNA1 induces microtubule nucleation and branching. We find that DIV2

474   neurons ectopically expressing *TUBA1A*-V409I or -V409A have increased levels of microtubule

475   acetylation, but not increased amounts of microtubule polymer (Figures 1B and 3C). Therefore,

476   our data suggest that V409I/A mutants are unique in that they behave similarly to taxol-treated

477   cells and do not promote increased nucleation compared to WT, but instead result in longer

478   lived microtubules that promote neurite branching.

479

480   Our results from modeling V409 mutants in budding yeast reveal the mechanistic origins of the

481   highly stable microtubules in neurons. We find that, compared to WT, *tub1/tub3*-V410I/A

482   microtubules have faster polymerization and depolymerization rates, decreased catastrophe

483   frequencies, and increased dynamicity (Figure 4). Dynamicity is calculated as the total change

484   in microtubule length (taking into account states of growth and shrinkage) divided by the change

485   in time (Jordan et al., 1993). It is interesting that despite the *tub1/tub3*-V410I/A microtubules

486   undergoing catastrophe less often than WT, they have increased dynamicity values. This

487   suggests that the increase in dynamicity is driven by increased polymerization and

488   depolymerization rates, as opposed to frequent transitions between the states of polymerizing

489   and depolymerizing. Accordingly, V410I/A microtubules reach longer lengths and are longer

490   lived. Assuming these dynamic parameters hold in neurons, longer microtubules that

491   catastrophe less often would result in increased microtubule acetylation, which is what we

492   observe in neurons expressing *TUBA1A*-V409I/A. Our data support a model in which the

493   V409I/A mutants promote excessive neurite branching similar to taxol-treated neurons, but alter

494   microtubule dynamics in a way that is distinct from the mechanisms of taxol.

495

496   Microtubule dynamics in cells are reliant on both extrinsic factors that interact with microtubules,

497   as well as intrinsic factors conferred by the tubulin heterodimer (Bodakuntla et al., 2019; Borys

498   et al., 2020; Goodson and Jonasson, 2018; Manka and Moores, 2018; Mitchison and Kirschner,

499   1984). One way in which tubulin heterodimers intrinsically control microtubule dynamics is by

500   adopting a series of conformations as microtubules polymerize and depolymerize (Chrétien et

501   al., 1995; Mandelkow et al., 1991). Free heterodimer exists in a kinked conformation, which

502   straightens out as the heterodimer is assembled into the microtubule lattice (Buey et al., 2006;

503   Jánosi et al., 1998; Nawrotek et al., 2011; Nogales and Wang, 2006; Ravelli et al., 2004; Rice et

504   al., 2008). We find that V410I/A tubulins have decreased affinity for Stu2 TOG1/TOG2 domains

505   in our *in vitro* binding assays (Figure 5C). Because Stu2 TOG domains preferentially bind to the

506   kinked conformation of the tubulin heterodimer, this raises the possibility that V410I/A mutants

507   push the heterodimer into a straightened conformation. Our finding that V410A increases the

508   rate of tubulin polymerization in the absence of extrinsic MAPs is also consistent with an effect

509   on tubulin's intrinsic conformation (Figure 6C). We propose a model in which tubulin

510   conformation acts more as a dial than an on and off switch (Figure 7). In this model, limiting the

511   range of conformations a heterodimer adopts is likely to affect the severity of the impact it has

512   on microtubule dynamics. Based off the results of our *in vitro* binding assays between tubulin

513   and Stu2 TOG1/2, V410I appears to have a milder effect on tubulin conformation as compared

514   to V410A (Figure 5C). We interpret this as that V410I can no longer adopt the full range of

515   conformations, but can adopt more of a kinked state than V410A, and thus has less drastic

516   effects on microtubule dynamics. In accordance with our prediction that V410I/A mutants are in

517   a straighter conformation than WT, we find that *tub1/tub3*-V410I microtubules, and more

518   significantly -V410A microtubules, have less Stu2 at their plus ends (Figure 5B). Additionally,

519   when Stu2 is conditionally depleted in cells, *tub1/tub3*-V410I/A microtubules are maintained

520   while WT microtubules are lost. Together, our data indicate that a consequence of limiting

521   tubulin conformational states is diminished regulation that is typically conferred by Stu2.

522

523   Tight control over microtubule dynamics is essential for cells, and particularly in neuron

524   morphogenesis and migration as the cytoskeletal must nimbly respond to cues throughout the

525   migratory process (Kapitein and Hoogenraad, 2015). XMAP215/Stu2 works in cells as an

526   extrinsic regulator to finely tune microtubule dynamics (Brouhard et al., 2008; Hahn et al., 2021;

527   Lee et al., 2001; van der Vaart et al., 2011; Vasquez et al., 1994; Zanic et al., 2013). The role of

528   XMAP215 in neurons has been explored primarily in the axon and growth cone. XMAP215's

529   polymerase activity is required for axon outgrowth and microtubule bundling, and in the growth

530   cone XMAP215 plays a role in linking microtubules and F-actin (Hahn et al., 2021; Lowery et al.,

531   2013; Slater et al., 2019). However, further studies should focus on the role XMAP215 plays in

532   neuron morphogenesis and migration, including in establishing neuron polarity and branching.

533   Beyond XMAP215/Stu2, which preferentially binds to the kinked conformation of tubulin, there

534   are numerous other microtubule-associated proteins that bind to a range of particular tubulin

535   conformations (Brouhard and Rice, 2018). Therefore, we predict that the activity of multiple

536   extrinsic regulators would be impacted by mutations that alter the conformational state of the

537   tubulin heterodimer. How these regulatory mechanisms are impacted by tubulin conformational

538   states and the subsequent effects of these changes on microtubule networks in cells will be a

539   major focus of future studies.

540

541   Our results, particularly for the V410A mutant, highlight how tubulin mutants can create

542   unexpected dissonance between extrinsic and intrinsic factors. Compared to WT tubulin, V410A

543   mutant tubulin promotes faster polymerization rates in cells and *in vitro*. It is interesting that in

544   our *in vitro* system, we were unable to identify a concentration at which homogeneous V410A

545   polymerizes from the GMPCPP-stabilized porcine tubulin seeds. However, blending V410A with

546   WT tubulin in a one-to-one ratio supports the assembly of microtubules with significantly

547   increased polymerization rates as compared to WT at the same concentrations of total tubulin.

548   This suggests that V410A may be unable to polymerize from GMPCPP seeds on its own, but it

549   drives fast polymerization when mixed with WT tubulin. Based on our data acquired from neuron

550   cultures, and particularly from budding yeast in which all the α-tubulin in the cell is V410A, we

551   know that this mutant assembles into microtubules that polymerize faster and are longer lived in

552   cells. Why then is V410A able to assemble into microtubules when it is the only source of α-

553   tubulin in the cell, but not when it is the only source of α-tubulin *in vitro*? One model we have

554   considered is that V410A disrupts the delicate equilibrium that exists between free tubulin

555   heterodimer, templated nucleation, and spontaneous nucleation. In cells there are factors such

556   as the γ-tubulin ring complex and various MAPs that promote tubulin nucleation into

557   microtubules. *In vitro*, our yeast tubulin must assemble on its own from GMPCPP-stabilized

558   porcine tubulin seeds. Our *in vitro* dynamics data indicate that when V410A is in a one-to-one

559   blend with WT, the x-intercept is similar to pure WT (Figure 6C). This indicates that the blend

560 would not be expected to nucleate at lower concentrations than WT alone. However, pure

561 V410A may have a lower critical concentration than WT and may shift the equilibrium toward

562 spontaneous nucleation away from stabilized seeds. However, when the mutant is blended with

563 WT, the WT may shift that equilibrium back and promote templated microtubule assembly.

564

565 Beyond V410A, interactions between different tubulin heterodimers (such as different mutants

566 or isotypes) is an important question to address both in regards to tubulinopathy disease as well

567 as normal tubulin biology. In tubulinopathy patients that harbor heterozygous mutations, the

568 mutant tubulin comprises at most 50% of either the α- or β-tubulin pool. This underscores the

569 necessity of future work to 1) determine the relative protein constituency of different tubulin

570 isotypes in different cell types, and 2) use blending experiments *in vitro* to recapitulate these

571 relative proportions. Additionally, this is an important consideration for furthering our

572 understanding of how normal tubulin biology works in cells. Using mutants that affect particular

573 intrinsic properties of tubulin (e.g. conformation, GTPase activity, etc.) in various blends with WT

574 tubulin will provide insight into how these different properties work in trans to alter microtubule

575 dynamics, and whether some mutants or isotypes might elicit outsized effects.

576

577 We propose a model in which the V409I/A mutants alter the conformational transitions of the

578 heterodimer and push it into a straighter state that drives faster microtubule dynamics and

579 ultimately perturb neuron morphologies and migration (Figure 7). An isoleucine or alanine

580 substitution at the valine 409 residue of *TUBA1A* seems relatively insignificant. However, these

581 subtle changes lead to drastic consequences that scale from altered microtubule dynamics to

582 an underdeveloped neocortex. Strikingly, *TUBA1A*-V409I presents an intermediate phenotype

583 between WT and *TUBA1A*-V409A in each assay we tested, tracking with the observed brain

584 malformations observed in these patients. To date, there are numerous missense, heterozygous

585 mutations in human tubulin genes that are associated with brain malformations, yet the

586 molecular mechanisms driving these tissue level defects remain unknown. Based off our work

587 and that of others, there does not appear to be a consistent mechanism for how *TUBA1A*

588 tubulinopathy mutations affect microtubule networks and neuron cell biology (Aiken et al., 2019;

589 Belvindrah et al., 2017; Gartz Hanson et al., 2016; Keays et al., 2007). The well-established

590 conformational dynamics of tubulin raise the possibility that mutations altering one region of the

591 heterodimer could allosterically affect distant regions, and thus disrupt the normal

592 conformational transitions that heterodimers undergo during assembly and disassembly.

593 Therefore, it is crucial to use quality genetic models to further our understanding of the

594 molecular mechanism of these patient-associated mutations. Additionally, our work highlights

595 the need for more detailed studies into how different regions of the tubulin heterodimer impact

596 tubulin conformational states, and how this affects extrinsic regulation that ultimately result in

597 altered microtubule dynamics. Investigating how subtle alterations in specific regions of the

598 heterodimer can have long ranging effects across microtubule networks will be a primary focus

599 of future work.

600

608

609 **MATERIALS AND METHODS**

610 *Animals*

611 Animal research was performed following regulations approved by the Institutional Animal Care

612 and Use Committee at the University of Colorado School of Medicine. All mouse tissue

613 experiments described below were from *C57BL6/J* wild-type pregnant mice (Jackson

614 Laboratories Strain #000664). All dissociated neuron cultures described below were prepared

615 from Sprague-Dawley rats. Dissociated cultures were obtained from both male and female

616 pups.

617

618 *TUBA1A plasmid vectors*

619 Plasmids used in this study are listed in Supplementary Table 1. The plasmids were constructed

620 using the methods described in Aiken et al. 2018. Briefly, the coding region of the human

621 *TUBA1A* gene was cloned into the multiple cloning site of the pCIG2 plasmid that express

622 cytoplasmic GFP from an internal ribosome entry site (IRES) (Hand et al., 2005). QuikChange

623 Lightning Site-Directed Mutagenesis Kit (Agilent Technologies, Santa Clara, CA) was used to

624 introduce either the p.V409A or p.V409I substitution into TUBA1A. All plasmids have the 6X-His

625 tag inserted between residues I42 and G43. Mutants were confirmed by sequencing. Oligos

626 used for plasmid constructions are listed in Supplementary Table 3.

627

628 *Primary Cortical Neuron Cultures*

629 The frontal cortex was dissected from postnatal days 0-2 male and female neonatal Sprague

630 Dawley rats. Cortices were digested at room temperature for 1 hour using papain solution

631 composed of 20 units/ml papain (Worthington Biochem, LS003126), 1.5 mM $CaCl_2$ (Sigma

632 Aldrich, 223506), 0.5 mM EDTA (Fisher Scientific, BP118-500), 1 mM NaOH (Fisher Scientific,

633 BP359-500), and 0.2mg/ml cysteine (Sigma Aldrich, C6852) in 10 ml saline. Digested cortices

634 were washed six time with Minimal Essential Media (MEM) (Life Technologies, Carlsbad, CA,

635 11090-081). Cortices were dissociated with a wide-bore fire-polished pipette, followed by

636 dissociation with a narrow-bore polished pipette. pCIG2-TUBA1A-His6 (either EV, WT, or

637 mutant) plasmids (4μg) were introduced to $4x10^6$ dissociated neurons using Amaxa rat

638 nucleofector kit (Lonza Bioscience, VPG-1003). Amaxa-nucleofected neurons plated at 500,000

639 cells per 35mm poly-D-lysine-coated glass bottom dish (WillCo Wells, HBST-3522) in MEM

640 containing 10% Fetal Bovine Serum (FBS) (Sigma Aldrich, F4135), 1% penicillin/streptomycin

641 (Gibco, 15070-063), and 25 μM L-glutamine (Gibco, 25030081). Following 2 hours in culture,

642 media was replaced with supplemented FBS. At 24 hours after plating, media was replaced with

643 Neurobasal-A (NBA) (Life Technologies, 10888-022), 2% B27 (Gibco, 17504-044), and 10 μM

644 uridine/fluoro-deoxyuridine (Sigma Aldrich, U3003/F0503). Neurons were maintained in a 37°C

645 humidified incubator with 5% CO_2.

646

647 *Neuron Immunocytochemistry*

648 Days in vitro (DIV) 2 or DIV3 primary cortical neurons were washed with phosphate buffered

649 saline (PBS) (Gibco, 10010023) followed by PHEM buffer, which contains 60 mM PIPES (Sigma

650 Aldrich, P6757), 25 mM HEPES (Sigma Aldrich, H3375), 10 mM EGTA (Sigma-Aldrich, E3889),

651 and 2 mM $MgCl_2$ (Acros, 223211000). Soluble tubulin dimers were extracted using 0.1% triton-X

652 (Sigma Aldrich, T9284) with 10 μM taxol (LC Labs, P-9600) and 0.1% DMSO (Fisher, M-1739)

653 in PHEM buffer. Cells were fixed with 4% paraformaldehyde (PFA) (Sigma Aldrich, 158127) and

654 0.1% glutaraldehyde (Sigma Aldrich, G7776) in PBS for 10 minutes at room temperature,

655 washed with PBS, then blocked with blocking buffer, 3% BSA (Fisher, 50-253-893) and 0.2%

656 Triton-X in PBS. Cells were reduced with 10 mg/ml sodium borohydride (Fisher, S678-10) in an

657 equal mixture of PBS and methanol (Acros, 177150050) for 7 minutes at room temperature,

658 then washed three times with PBS. Cells were incubated with blocking buffer for 20 minutes at

659 room temperature. Immunostaining was performed using a primary antibody directed against

660 6X-Histidine (Invitrogen, 4A12E4 37-2900; 1:500), beta-II tubulin (Abcam, ab179512; 1:500),

661 acetylated tubulin (Sigma, T7451; 1:1000), tyrosinated tubulin (Sigma, MAB1864-I; 1:1000).

662   Primary antibody was diluted in blocking buffer and incubated overnight at 4ºC in a humidified

663   chamber. After primary antibody staining, cells were washed three times with PBS. The

664   secondary antibodies goat anti-rabbit IgG Alexa Fluor 568 (Thermo, A-11011), goat anti-rat IgG

665   Alexa Fluor 568 (Thermo, A-11077), or goat anti-mouse IgG Alexa Fluor 647 (Thermo, A32728)

666   were diluted 1:200 in blocking buffer and 1% normal goat serum (Vector Laboratories, S-1000-

667   20) and incubated for 2 hours at room temperature in a dark container. Cells were sealed with

668   glass coverslips and aqueous mounting media containing DAPI (Vector Laboratories, H-1200),

669   then imaged on a spinning disk confocal microscope with a 40x oil objective (see details below).

670   Statistical analysis between multiple groups were analyzed by two-way ANOVA and analyzed

671   *post hoc* by Tukey test.

672

673   *In utero electroporation*

674   *In utero* electroporations were performed on E14.5 embryos of *C57BL6/J* wild-type pregnant

675   mice. Plasmid DNA was endotoxin-free and prepared with 0.1% fast green dye and had a final

676   concentration of 1µg/µl in TE buffer (10mM Tris base and 1mM EDTA, pH 8.0). Plasmid DNA

677   was injected into the lateral ventricles of the exposed embryos and electroporated with 5 pulses

678   at 50V for 100ms pulses each, separated by 950ms. All embryos developed to E18.5, then

679   brains were dissected and fixed overnight at 4˚C in 4% paraformaldehyde. A vibrating

680   microtome (VT1200S; Leica, Buffalo Grove, IL) was used for 50µm thick coronal sections.

681   Sections were mounted on glass slides, then imaged on a spinning disk confocal microscope

682   with a 20x objective. Analysis includes at least three animals, both male and female, per

683   condition.

684

685   *Neuron cold temperature shock*

686   The media of DIV2 neuron cultures (as described above) was replaced with Neurobasal-A

687   (NBA) (Life Technologies, 10888-022), 2% B27 (Gibco, 17504-044), and 10 µM uridine/fluoro-

688   deoxyuridine (Sigma-Aldrich, U3003/F0503). The dishes were then placed at 4˚C for the desired

689   time. At each time point, dishes were removed from 4˚C and placed on ice while following the

690   fixing protocol described above.

691

692   *Neuron morphology and post-translational modifications analysis*

693   All images were analyzed using ImageJ (National Institute of Health) and the NeuronJ plugin

694   (Meijering et al., 2004). Neuron processes were defined as primary, secondary, or tertiary, then

695   quantified for each cell analyzed. Post-translational modification fluorescent signals were

696   quantified from each cell by measuring line scans along processes. For consistency within each

697   individual cell, the line scans were first traced using cytoplasmic GFP signal, saved, and then

698   used to measure signal from the immunofluorescent staining for the tubulin PTMs in different

699   channels. A two-way ANOVA analyzed *post hoc* by Tukey test was used for statistical analyses

700   between multiple groups.

701

702   *Yeast microtubule dynamics*

703   Microtubule dynamics were analyzed in log-phase, pre-anaphase yeast cells in which all the α-

704   tubulin in the cell was either WT, V410I, or V410A. The mutants were integrated at the native

705   *TUB1* and *TUB3* loci. Microtubule plus-ends were identified by Bik1-3GFP. Images were

706   collected on a Nikon Ti-E microscope equipped with a 1.45 NA 100✕ CFI Plan Apo objective,

707   piezo electric stage (Physik Instrumente, Auburn, MA), spinning disk confocal scanner unit

708   (CSU10; Yokogawa), 488-nm and 561-nm lasers (Agilent Technologies, Santa Clara, CA), and

709   an EMCCD camera (iXon Ultra 897; Andor Technology, Belfast, UK) using NIS Elements

710   software (Nikon). Cells were grown asynchronously to early log phase in nonfluorescent media

711   and adhered to slide chambers coated with concanavalin A. Slide chambers were sealed with

712   VALAP (Vaseline, lanolin and paraffin at 1:1:1). Z-series consisting of a 7μm range at 0.4μm

713   steps were acquired every 4 seconds for 10 minutes at 30˚C. Astral microtubule lengths were

714   measured in each frame as the distance from the spindle pole body to the microtubule plus-end.

715   Cell genotypes were blinded for analysis. Statistical analysis was done using a one-way ANOVA

716   followed by a Tukey test to correct for multiple comparison tests.

717

718   *Stu2 localization*

719   Analysis was done in log-phase, pre-anaphase budding yeast cells expressing either *tub1/tub3-*

720   WT, V410I, or V410A, as well as Stu2-3GFP. The tubulin mutations and the fluorescent tagging

721   of Stu2 were done at the endogenous loci. Short time-lapse images, every 5 seconds for 30

722   seconds, were collected on a spinning disc confocal microscope with a 100x oil objective, using

723   Z-series consisting of 0.4μm steps over a total range of 7μm. Stu2-3GFP fluorescence intensity

724   was measured at the plus-ends of growing astral microtubules by defining a 182nm^2 region. A

725   region of the same size and adjacent to the Stu2-3GFP foci was also measured and subtracted

726   from the Stu2-3GFP intensity value to account for background fluorescence. Statistics represent

727   values from a one-way ANOVA corrected for multiple comparison by a Tukey test.

728

729   *GST-TOG1/2 purification*

730   Purification of GST-TOG1/2 followed previously described methods and is described briefly

731   below (Reusch et al., 2020; Widlund et al., 2012). The pGEX-6P-1 Stu2 1-590 plasmid was

732   transformed into BL21 cells and colonies were grown on an LB plate containing 100µg/ml

733   carbenicillin and 15µg/ml chloramphenicol at 37°C. A colony was inoculated overnight at 37°C

734   in MDAG-135 media (25mM Na_2HPO_4, 25mM KH_2PO_4, 50mM NH_4Cl, 5mM Na_2SO_4, 2mM

735     $MgSO_4$, 0.2x metals, 0.35% glucose, 0.1% aspartate, 200µg/ml each of 18aa (no C, Y))

736   containing 100µg/ml carbenicillin and 15µg/ml chloramphenicol (Studier, 2005). The following

737   day the colony was diluted 500-fold in 1L of Terrific Broth media (Fisher, BP2468-2) with

738   100µg/ml carbenicillin and 15µg/ml chloramphenicol and grown at 37°C until the OD_{600} reached

739   approximately 0.5. The cultures were shaken at 18°C for 1 hour, then induced with 0.2mM

740   isopropyl β-$_D$-1-thiogalactopyranoside for 18 hours (Fisher, BP1620-1). Following induction cells

741   were pelleted at 6,200xg for 10 minutes at 6°C and resuspended in a 1:1 ratio with a buffer

742   consisting of 2X phosphate-buffered saline (PBS), 1mM dithiothreitol (DTT), 20µl benzonase

743   (25U/µl), and 1X protease inhibitors (2 cOmplete EDTA-free Tablets per 100ml; Roche,

744   04693132001). The cells were lysed by two passes through a microfluidizer at 1,500 bar. Cell

745   lysate was then clarified by spinning at 12,000rpm for 30 minutes at 4°C.

746

747   A 5mL GSTrap HP column (GE, 17-5282-01) was preequilibrated with 5 column volumes (CV)

748   of wash buffer (2X PBS, 1mM DTT) at 1mL/min. The clarified lysate was then loaded onto the

749   column at 0.5mL/min. The following washes were all done at 1mL/min. The column was washed

750   with 10CV of wash buffer with 0.1% Tween 20, then 2CV of 2X PBS with 5mM ATP and 10mM

751     $MgCl_2$. The column incubated in this buffer for 20 minutes. The column was then washed with

752   5CV of 6X PBS, followed by 5CV of wash buffer. GST-TOG1/2 was eluted from the column in

753   1mL fractions into a deep 96-well plate with wash buffer plus 5mM reduced glutathione, pH 8.0.

754   The eluted fractions were run on a gel and stained with Coomassie. Fractions containing GST-

755   TOG1/2 were pooled and dialyzed against three changes (after 2h, overnight, then another 2h)

756   of coupling buffer (100mM NaHCO3, 100mM NaCl, pH 8.2) at 4°C. The dialyzed sample was

757   concentrated in 0.5ml centrifuge concentrating filters (Sigma Z677108) that had been

758   preequilibrated with coupling buffer. GST-TOG1/2 was concentrated to 14.5µM and stored in

759   25µl aliquots at -80°C.

760

761   *Yeast tubulin purification*

762   Purification of yeast tubulin was based on previously described methods with slight

763   modifications (Minoura et al., 2013). Protease deficient yeast cells (JEL1) were transformed with

764   pRS426-GAL-Tub1-internal 6X-His and pRS424-GAL-Tub2 (untagged). tub1-V410I and -V410A

765   mutants were constructed in the pRS426-GAL-Tub1-internal 6X-His plasmid with QuikChange

766   XL. Cells were grown in five or six 5ml cultures of selection media (-ura -trp) supplemented with

767   2% glucose for either three or two days, respectively, at 30°C. 5ml cultures were then

768   transferred to 50ml cultures of the same media to grow for 24 hours. Cultures were then

769   transferred to 1L cultures of YPGL, consisting of 10g yeast extract (Fisher, BP1422), 20g

770   peptone (Fisher, BP1420), 30ml glycerol (Fisher, G33), and 33ml lactate (Sigma, L1375). Yeast

771   extract, peptone, and 850ml ddH$_2$O was combined and autoclaved the day before it was

772   needed. The glycerol and lactate were added immediately after media came out of the

773   autoclave, then allowed to cool at room temperature overnight. After 20-24 hours of growing in

774   1L cultures and the OD600 was between 5.0-9.0, 1L of cells was induced with 20g galactose

775   (Chem-Impex, 01449) for five hours. Cells were spun down at 4°C for 15 minutes at 4000 RPM

776   (3040 RCF) in a J6 centrifuge (Beckman Coulter Life Sciences). Supernatant was discarded

777   and pellets were stored in 15ml conical tubes in -80°C. This process was done three times for a

778   total of approximately 100g of cells before moving on to purification.

779

780   Cell pellets were thawed on ice and combined with cold lysis buffer (50mM HEPES, 500mM

781   NaCl, 10mM MgSO$_4$, 30mM Imidazole) plus freshly added 50µm GTP (Sigma G8877) and 1mM

782   PMSF (Acros Organics, 215740050) to a total of approximately 150ml. While cells were

783   thawing, the microfluidizer (Microfluidics, M-110P) was packed with ice to cool. Cells were

784   passed through the microfluidizer four times at 27,000 PSI with 10 minutes on ice between each

785   pass. The cells were chased with 50ml lysis buffer supplemented with 50µM GTP and 1mM

786   PMSF. The lysed cells were clarified in an Avanti J-26S XPI centrifuge (Beckman Coulter Life

787   Sciences) at 41,000 RCF for 30 minutes at 4°C. The pellets were discarded and the supernatant

788   was applied to a 5ml His60 Ni column (Takara, 635680) that was pre-equilibrated with 20

789   column volumes of lysis buffer. The column was washed with 10 column volumes of lysis buffer

790   supplemented with 50µM GTP, then with 10 column volumes of wash buffer (25mM PIPES pH

791   6.9, 1mM MgSO$_4$, 30mM Imidazole, 200mM NaCl) with 50µM GTP. Protein was eluted from the

792   column with 10 column volumes of elution buffer (25mM PIPES pH 6.9, 1mM MgSO$_4$, 300mM

793   Imidazole, 200mM NaCl) with 50µM GTP into 2 x 5ml samples followed by 4 x 10ml samples.

794   Samples from the wash and elution steps were run on a gel and Coomassie staining was used

795   to determine which fractions contained tubulin. Elution fractions with tubulin were pooled and

796   20% glycerol was added before flash freezing the samples in liquid nitrogen and storing at -

797   80°C.

798

799 Elution fractions from the Ni column were thawed in a room temperature water bath and 10µl of

800 nuclease (Pierce, 88701) was added per 25ml of sample, then sat for one hour at room

801 temperature. Two HiTrap Q HP 1ml columns (GE, 17-1153-01) were strung together on an

802 AKTA FPLC (GE) and equilibrated with 10 column volumes (20ml) of ddH$_2$O, 5 column volumes

803 of Buffer A (25mM PIPES pH 6.9, 2mM MgSO$_4$, 1mM EGTA), 5 column volumes of Buffer B

804 (25mM PIPES pH 6.9, 2mM MgSO$_4$, 2mM EGTA, 1M NaCl), and 10 column volumes of Buffer

805 A, all run at 1ml/min. The column was then equilibrated at 2ml/min with 12.5 column volumes of

806 80% Buffer A and 20% Buffer B, both supplemented with 50µM GTP. Sample from Ni column

807 was injected into a 50ml Superloop that was washed with diH$_2$O followed by Buffer A. The

808 sample was applied to the column at 0.5ml/min using Buffer A. Once the sample was loaded the

809 tubulin was eluted with 30 column volumes of Buffer A and a 20-60% gradient of Buffer B, both

810 supplemented with 50µM GTP. Elution was collected in 0.5ml fractions in a 96 deep-well plate.

811 Elution fractions were run on a gel and Coomassie staining determined which fractions had pure

812 tubulin and would be used to concentrate the protein.

813

814 Amicon ultra 0.5ml centrifuge concentrating filters with a 10kDa cutoff (Sigma, Z677108) were

815 prepared with two rounds of 0.4ml 1% Triton X-100, ddH$_2$O, and PEM (0.1M PIPES, 1mM

816 EGTA, 1mM MgCl$_2$) spinning at 800 RCF for 5 minutes at 4°C. Up to 0.450ml of pure tubulin

817 sample was applied to the concentrating filters and spun at 4°C at 800 RCF for anywhere

818 between 2-5 minutes, depending on the concentration of the sample. The concentration was

819 checked after each spin on a Take3 Micro-volume Plate (BioTek) using 260nm and 280nm

820 absorbance to ensure that the concentration was increasing but aggregates were not forming.

821 Samples were constantly kept on ice or at 4°C and concentrated to 2.2µM (tub1-V410I), 2.3µM

822 (tub1-V410A), and 3µM (TUB1). Concentrated protein samples were run through a Zeba spin

823 2ml desalting column (Thermo, 89890) that was prepared by spinning at 1000 RCF for 2

824 minutes at 4°C to remove storage buffer, then washed three times with 0.4ml PEM. Up to 0.7ml

825 of concentrated sample was added to each desalting column, then spun down at 1000 RCF for

826 2 minutes at 4°C. The flow-through sample was supplemented with 50µM GTP, aliquoted into

827 20µl samples that were flash frozen in liquid nitrogen, and stored at -80°C. At least two separate

828 rounds of purifications were used as technical replicates for *in vitro* assays that used this

829 purified tubulin.

830

831 *TOG binding assay*

832   Pierce Glutathione Magnetic Agarose Beads (Thermo, 78602) were used to separate purified

833   GST-TOG1/2 (above) and anything bound in complex with TOG1/2 from the rest of the reaction.

834   100µl of bead slurry (equates to 25µl settled beads) were equilibrated twice with 40µl wash

835   buffer (125mM Tris-HCl, 150mM KCl, 1mM DTT, 1mM EDTA, pH 7.4) by vortexing for 10

836   seconds and removing buffer by placing tube on magnetic stand. In separate tubes, 100nM

837   tubulin (WT, V410I, or V410A; purification described above) was mixed with a range of GST-

838   TOG1/2 concentrations (from 9.8nM to 5µM) at 4°C for 15 minutes. Reaction was added to the

839   equilibrated beads and rotated at 4°C for 1 hour. Tubes were placed on magnetic stand and

840   supernatant was collected. The supernatant was prepared with Laemmli sample buffer and β-

841   mercaptoethanol and loaded onto a 10% SDS-PAGE gel. The gel was transferred to a PVDF

842   membrane (Millipore, IPFL85R), blocked with a PBS Blocking Buffer (LI-COR, 927-70001) at

843   room temperature for 1 hour, and probed with mouse anti-α-tubulin (4A1; 1:100) or mouse anti-

844   β-tubulin (E7; 1:100) overnight at 4°C. The following day the membranes were washed once for

845   5 minutes with 1X PBS, then incubated at room temperature in the dark for 1 hour with goat

846   anti-mouse-680 (LI-COR, 926-68070; 1:15,000). Membranes were washed twice with 1X PBST,

847   then once with 1X PBS before imaging on an Odyssey Imager (LI-COR, 2471). Both α- and β-

848   tubulin band intensity was analyzed using Image Studio v5.2 (LI-COR). Tubulin band intensity

849   represents the amount of tubulin in solution that is not bound to GST-TOG1/2.

850

851   *Stu2 depletion and yeast immunofluorescence*

852   Stu2 depletion strains originally constructed from Kosco et al. were graciously gifted from Dr.

853   Tim Huffaker (Kosco et al., 2001). Strains were modified to mutate the endogenous *TUB1* locus

854   to either V410I or V410A using site-directed mutagenesis. Cells were grown to log-phase, then

855   induced with 500µM cupric sulfate for 1.5 hours at 30°C. The following fix and staining protocol

856   was adapted from (Miller, 2004) as described. Cells were fixed with 3.7% formaldehyde (Sigma-

857   Aldrich, 252549) at 30°C for 2 hours, then spun down at 3000RPM for 3 minutes. Pellet was

858   washed twice with wash buffer (40mM KPO_4, pH 6.5), then stored overnight at 4°C. The pellet

859   was washed twice with wash buffer plus 1.2M sorbitol. Fixed cells were digested with 10µl of

860   20T 50mg/ml zymolyase (Nacali Tesque, 07663-91) and 15µl β-mercaptoethanol (Sigma-

861   Aldrich, M3148) for 45 minutes at 37°C. Digested cells were spun down at 2000RPM for 3

862   minutes, washed once with wash buffer plus 1.2M sorbitol, then resuspended in 20µl wash

863   buffer plus 1.2M sorbitol. 20µl of cells were spotted onto each well of a Teflon coated 10 well

864   slide (Polysciences, 18357) that had been pre-treated with 10ng/µl poly-L-lysine. Cells adhered

865   for 10 minutes at room temperature. Liquid was aspirated off before immediately permeabilizing

866   the cells in a coplin jar of cold methanol for 6 minutes, followed by immersing the slide in cold

867   acetone for 30 seconds. Cells were blocked at room temperature for 1 hour in blocking buffer

868   (1X PBS + 0.5% BSA), then incubated overnight at 4°C in a humid chamber with mouse anti-α-

869   tubulin (4A1; 1:100 in blocking buffer). Wells were washed 4 times for 10 minutes with blocking

870   buffer, then incubated at room temperature for 1 hour in a dark humid chamber with goat anti-

871   mouse IgG-Alexa488 (Invitrogen, A11001). Cells were washed 4 more times with blocking

872   buffer. DAPI mounting solution (Vector Laboratories, H-1200) was added to the slide, then

873   imaged on widefield microscope with a 100x oil objective. Statistical analysis was done using a

874   two-way ANOVA corrected for multiple comparison by a Tukey test.

875

876   *Yeast growth assays*

877   For liquid growth assays, saturated cultures were diluted 1:500 in rich media. In a 96-well plate

878   200µl/well was used. OD600 values were measured on an Epoch 2 Microplate

879   Spectrophotometer (BioTek #EPOCH2NS) every 5 minutes for at least 19 hours at 30°C with

880   orbital shaking. The doubling time was calculated by fitting the measured OD600 values to an

881   exponential curve using a MATLAB code that has previously been described (Fees et al., 2016).

882   The doubling times have been normalized to WT cells. A two-way ANOVA was used to compare

883   across multiple groups and corrected *post hoc* by a Tukey test.

884

885   *4°C temperature shock in yeast*

886   Cells expressing either TUB1/TUB3, tub1/tub3-V410I, or tub1/tub3-V410A along with GFP-

887   Tub1, GFP-Tub1-V410I, or GFP-Tub1-V410A, respectively, were grown overnight at 30°C in

888   rich liquid media. The following day the cells were diluted in fresh media and grown to log

889   phase. The log phase cultures were then transferred to a shaker at 4°C for the indicated amount

890   of time. Cells were fixed at 4°C with 3.7% formaldehyde and 0.1M KPO_4 for three minutes. Cells

891   were pelleted on a desktop centrifuge and supernatant was discarded. The pellet was

892   resuspended in quencher solution (0.1% Triton-X, 0.1M KPO_4, 10mM ethanolamine). The cells

893   were pelleted and washed twice with 0.1M KPO_4. Imaging chamber slides were coated with

894   concanavalin A and washed with 0.1M KPO_4 before loading fixed cells into the chambers and

895   sealed with VALAP (Vaseline, lanolin, and paraffin at a 1:1:1 ratio) (Fees and Moore, 2018).

896

897   *In vitro dynamics analysis using interference reflection microscopy*

898   Interference reflection microscopy was used to measure microtubule dynamics of unlabeled

899   purified tubulin. Chambers were assembled with two different sized coverslips, 22mm x 22mm

900 and 18mm x 18mm, that were silanized and plasma cleaned. Three strips of single ply parafilm

901 were melted between the coverslips to create two chambers on a custom-made stage insert.

902 Anti-rhodamine antibody (Life Technologies, A6397) was diluted 1:100 in cold BRB80 (80mM

903 PIPES, 1mM $MgSO_4$, 1mM EGTA), flowed into the chamber, then sat at room temperature for

904 five minutes. The antibody was then washed out with room temperature BRB80. Chambers

905 were flushed with 1% pluornic-F127 in BRB80 and incubated in this buffer for five minutes, then

906 washed out with room temperature BRB80. The stage insert was placed in the scope enclave to

907 equilibrate at 30°C for 30 minutes. GMPCPP-stabilized microtubule seeds that attached to the

908 anti-rhodamine antibody on the coverslips were flowed into the chamber where they settled for

909 30 seconds before washing out with room temperature BRB80. The chambers were washed

910 with reaction buffer that contained no tubulin (1X PEM, 0.1% methyl cellulose, 1mM GTP,

911 0.1mg/ml BSA) before adding the reaction buffer along with 0.3µM-0.9µM tubulin. The chamber

912 was then sealed with VALAP. The reaction in the chamber was equilibrated on the widefield

913 microscope for 20 minutes at 30°C to prevent drifting during imaging. Following the equilibration

914 period, images were collected every second for one hour in the interference reflection

915 microscopy channel (MAHAMDEH et al., 2018). The 561nm channel was also collected for the

916 first frame to mark the GMPCPP-stabilized seeds. ImageJ was used for analyzing microtubule

917 dynamics by generating kymographs of individual microtubules.

918

919 **Supplementary Table 1. Plasmids**

Plasmid ID	Plasmid Name	Source
pJM0157	pGEX6p1-GST-STU2 1-590	Widlund et al. 2012
pJM0295	pCIG2	Hand et al. 2005
pJM0288	pRS426-GAL-Tub1-internal 6Xhis	Johnson et al. 2011
pJM0289	pRS424-GAL-Tub2 (untagged)	Johnson et al. 2011
pJM459	Stu2-3GFP	This study
pJM0469	TUB1-pRS306 integrating plasmid	Aiken et al. 2020
pJM507	Tub1-V410I-pRS306 integrating plasmid	This study
pJM560	Tub1-V410A-pRS306 integrating plasmid	This study
pJM0546	pCIG2-TUBA1A-6XHis	Buscaglia et al. 2020a
pJM0558	pRS426-GAL-Tub1(V410A)-internal 6Xhis	This study
pJM0559	pRS426-GAL-Tub1(V410I)-internal 6Xhis	This study
pJM0612	pCIG2-TUBA1A(V409I)-int-6XHis	This study
pJM0642	pCIG2-TUBA1A(V409A)-int-6XHis	This study

920

921 **Supplementary Table 2. Yeast strains**

Yeast Strain	Genotype	Source
yJM3733	MATα tub1::pJM469(TUB1 +487::URA) Stu2-3GFP::TRP ura3-52 lys2-801 leu2-Δ1 his3-Δ200 trp1-Δ63	This study
yJM3734	MATa tub1::pJM469(TUB1 +487::URA) Stu2-3GFP::TRP ura3-52 lys2-801 leu2-Δ1 his3-Δ200 trp1-Δ63	This study
yJM4010	MATa BIK1-3GFP::TRP1 tub1::pJM560(TUB1-V410A +487::URA) tub3-V410A+150::hygB ura3-52 lys2-801 leu2-Δ1 his3-Δ200 trp1-Δ63	This study
yJM4011	MATα BIK1-3GFP::TRP1 tub1::pJM560(TUB1-V410A +487::URA) tub3-V410A+150::hygB ura3-52 lys2-801 leu2-Δ1 his3-Δ200 trp1-Δ63	This study
yJM4014	MATa BIK1-3GFP::TRP1 tub1::pJM507(TUB1-V410I +487::URA) tub3-V410I+150::hygB ura3-52 lys2-801 leu2-Δ1 his3-Δ200 trp1-Δ63	This study

yJM4015	MATα BIK1-3GFP::TRP1 tub1::pJM507(TUB1-V410I +487::URA) tub3-V410I+150::hygB ura3-52 lys2-801 leu2-Δ1 his3-Δ200 trp1-Δ63	This study
yJM4077	MATa STU2-3GFP::TRP1 tub1::pJM560(TUB1-V410A +487::URA) tub3-V410A+150::hygB ura3-52 lys2-801 leu2-Δ1 his3-Δ200 trp1-Δ63	This study
yJM4078	MATα STU2-3GFP::TRP1 tub1::pJM560(TUB1-V410A +487::URA) tub3-V410A+150::hygB ura3-52 lys2-801 leu2-Δ1 his3-Δ200 trp1-Δ63	This study
yJM4081	MATa STU2-3GFP::TRP1 tub1::pJM507(TUB1-V410I +487::URA) tub3-V410I+150::hygB ura3-52 lys2-801 leu2-Δ1 his3-Δ200 trp1-Δ63	This study
yJM4082	MATα STU2-3GFP::TRP1 tub1::pJM507(TUB1-V410I +487::URA) tub3-V410I+150::hygB ura3-52 lys2-801 leu2-Δ1 his3-Δ200 trp1-Δ63	This study
yJM4726	MATα tub1::pJM469(TUB1 +487::URA) TUB3+150::hygB BIK1-3GFP::TRP1 ura3-52 lys2-801 leu2-Δ1 his3-Δ200 trp1-Δ63	This study
yJM4727	MATa tub1::pJM469(TUB1 +487::URA) TUB3+150::hygB BIK1-3GFP::TRP1 ura3-52 lys2-801 leu2-Δ1 his3-Δ200 trp1-Δ63	This study
yJM4835	MATa PACE1-UBR1 PACE1-ROX1 stu2Δ::URA3::PANB1-UB-R-STU2 ura3-52 trp1-Δ1 ade2-101 lys2-801	Kosco et al. 2001
yJM4836	MATa PACE1-UBR1 PACE1-ROX1 ura3-52::URA3 ura3-52 trp1-Δ1 ade2-101 lys2-801	Kosco et al. 2001
yJM4859	MATa PACE1-UBR1 PACE1-ROX1 stu2Δ::URA3::PANB1-UB-R-STU2 tub1::pJM754(TUB1 +487::TRP1) ura3-52 trp1-Δ1 ade2-101 lys2-801	This study
yJM4860	MATa PACE1-UBR1 PACE1-ROX1 stu2Δ::URA3::PANB1-UB-R-STU2 tub1-V410I::pJM755(TUB1+487-V410I::TRP1) ura3-52 trp1-Δ1 ade2-101 lys2-801	This study
yJM4861	MATa PACE1-UBR1 PACE1-ROX1 stu2Δ::URA3::PANB1-UB-R-STU2 tub1-V410A::pJM756(TUB1+487-V410A::TRP1) ura3-52 trp1-Δ1 ade2-101 lys2-801	This study

922
923 **Supplementary Table 3. Oligo sequences (5' to 3')**

#	Name	Application	Sequence	Species	Direction
674	TUBA1A-V409A F QC	TUBA1A-V409A F Quikchange	ctttgttcactggtacgctggggaggggatg	Human	Forward
675	TUBA1A-V409A R QC	TUBA1A-V409A R Quikchange	catcccctcccagcgtaccagtgaacaaag	Human	Reverse
986	TUBA1A-V409I F QC	TUBA1A-V409I F Quikchange	cctttgttcactggtacattggggaggggatgg	Human	Forward
987	TUBA1A-V409I R QC	TUBA1A-V409I R Quikchange	ccatcccctccccaatgtaccagtgaacaaagg	Human	Reverse
1042	TUBA1A Gibson PstI insert F	Amplify TUBA1A from pINCY into pCIG2	ctcaagcttcgaattctgcaATGcgtgagtgcatctccatcc	Mouse	Forward
1043	TUBA1A Gibson PstI insert R	Amplify TUBA1A from pINCY into pCIG2	cggtaccgtcgactgcaTTAgtattcctctccttcttcctcaccc	Mouse	Reverse
1075	TUBA1A-T349E F QC	TUBA1A-T349E F Quikchange	gtttgtggattggtgccccgagggcttcaaggttggcatca	Human	Forward
1076	TUBA1A-T349E R QC	TUBA1A-T349E R Quikchange	tgatgccaaccttgaagccctcggggcaccaatccacaaac	Human	Reverse
867	pCIG2-TUBA1A stop + 53 R	TUBA1A sequencing	GGCTTCGGCCAGTAACGTTAG	Mammalian	Reverse
868	pCIG2-TUBA1A start – 52 F	TUBA1A sequencing	CCTACAGCTCCTGGGCAACG	Mammalian	Forward
545	tub1-V410A F	tub1-V410A F Quikchange	CGTCCACTGGTATGCCGGTGAAGGTATG	Yeast	Forward
546	tub1-V410A R	tub1-V410A R Quikchange	CATACCTTCACCGGCATACCAGTGGACG	Yeast	Reverse
1018	tub1-V410I F	tub1-V410I F Quikchange	cgtgctttcgtccactggtatatcggtgaaggt	Yeast	Forward

1019	tub1-V410I R	tub1-V410I R Quikchange	accttcaccgatataccagtggacgaaagcacg	Yeast	Reverse
1280	tub3-V410A F	tub3-V410A F to introduce mutation at TUB3 locus	TGATGTATGC CAAACGTGCT TTCGTCCATT GGTAT GcC GGTGAAGGTATG GAAGAAGGTG	Yeast	Forward
1281	tub3-V410I F	tub3-V410I F to introduce mutation at TUB3 locus	TGATGTATGC CAAACGTGCT TTCGTCCATT GGTAT aTC GG TGAAGGTATG GAAGAAGGTG	Yeast	Forward
5551	TUB3 + 154 R	To introduce V410 mutations at TUB3 locus	GCTATTGTTCTAACTGTACACCTAAAGGTAAGTG gca tag gcc act agt gga tc	Yeast	Reverse

924

References

926

927 Aiken J, Buscaglia G, Aiken AS, Moore JK, Bates EA. 2020. Tubulin mutations in brain
928   development disorders: Why haploinsufficiency does not explain TUBA1A
929   tubulinopathies. *Cytoskeleton* **77**:40–54. doi:10.1002/cm.21567
930 Aiken J, Moore JK, Bates EA. 2019. TUBA1A mutations identified in lissencephaly patients
931   dominantly disrupt neuronal migration and impair dynein activity. *Hum Mol Genet*
932   **28**:1227–1243. doi:10.1093/hmg/ddy416
933 Al-Bassam J, Kim H, Flor-Parra I, Lal N, Velji H, Chang F. 2012. Fission yeast Alp14 is a dose-
934   dependent plus end-tracking microtubule polymerase. *Mol Biol Cell* **23**:2878–2890.
935   doi:10.1091/mbc.E12-03-0205
936 Ayaz P, Munyoki S, Geyer EA, Piedra F-A, Vu ES, Bromberg R, Otwinowski Z, Grishin NV,
937   Brautigam CA, Rice LM. 2014. A tethered delivery mechanism explains the catalytic
938   action of a microtubule polymerase. *Elife* **3**:e03069–e03069. doi:10.7554/eLife.03069
939 Ayaz P, Ye X, Huddleston P, Brautigam CA, Rice LM. 2012. A TOG:αβ-tubulin Complex Structure
940   Reveals Conformation-Based Mechanisms for a Microtubule Polymerase. *Science*
941   **337**:857. doi:10.1126/science.1221698
942 Bahi-Buisson N, Poirier K, Fourniol F, Saillour Y, Valence S, Lebrun N, Hully M, Fallet Bianco C,
943   Boddaert N, Elie C, Lascelles K, Souville I, LIS-Tubulinopathies Consortium, Beldjord C,
944   Chelly J. 2014. The wide spectrum of tubulinopathies: what are the key features for the
945   diagnosis? *Brain* **137**:1676–1700. doi:10.1093/brain/awu082
946 Barkovich AJ, Guerrini R, Kuzniecky RI, Jackson GD, Dobyns WB. 2012. A developmental and
947   genetic classification for malformations of cortical development: update 2012. *Brain*
948   **135**:1348–1369. doi:10.1093/brain/aws019
949 Barkovich AJ, Kuzniecky RI, Jackson GD, Guerrini R, Dobyns WB. 2005. A developmental and
950   genetic classification for malformations of cortical development. *Neurology* **65**:1873.
951   doi:10.1212/01.wnl.0000183747.05269.2d
952 Basnet N, Nedozralova H, Crevenna AH, Bodakuntla S, Schlichthaerle T, Taschner M, Cardone G,
953   Janke C, Jungmann R, Magiera MM, Biertümpfel C, Mizuno N. 2018. Direct induction of
954   microtubule branching by microtubule nucleation factor SSNA1. *Nat Cell Biol* **20**:1172–
955   1180. doi:10.1038/s41556-018-0199-8
956 Belvindrah R, Natarajan K, Shabajee P, Bruel-Jungerman E, Bernard J, Goutierre M, Moutkine I,
957   Jaglin XH, Savariradjane M, Irinopoulou T, Poncer J-C, Janke C, Francis F. 2017. Mutation

958   of the α-tubulin Tuba1a leads to straighter microtubules and perturbs neuronal
959   migration. *J Cell Biol* **216**:2443–2461. doi:10.1083/jcb.201607074

960 Bodakuntla S, Jijumon AS, Villablanca C, Gonzalez-Billault C, Janke C. 2019. Microtubule-
961   Associated Proteins: Structuring the Cytoskeleton. *Trends in Cell Biology* **29**:804–819.
962   doi:10.1016/j.tcb.2019.07.004

963 Borys F, Joachimiak E, Krawczyk H, Fabczak H. 2020. Intrinsic and Extrinsic Factors Affecting
964   Microtubule Dynamics in Normal and Cancer Cells. *Molecules* **25**:3705.
965   doi:10.3390/molecules25163705

966 Breton S, Brown D. 1998. Cold-induced microtubule disruption and relocalization of membrane
967   proteins in kidney epithelial cells. *J Am Soc Nephrol* **9**:155. doi:10.1681/ASN.V92155

968 Brouhard GJ, Rice LM. 2018. Microtubule dynamics: an interplay of biochemistry and
969   mechanics. *Nat Rev Mol Cell Biol* **19**:451–463. doi:10.1038/s41580-018-0009-y

970 Brouhard GJ, Stear JH, Noetzel TL, Al-Bassam J, Kinoshita K, Harrison SC, Howard J, Hyman AA.
971   2008. XMAP215 is a processive microtubule polymerase. *Cell* **132**:79–88.
972   doi:10.1016/j.cell.2007.11.043

973 Buey RM, Díaz JF, Andreu JM. 2006. The Nucleotide Switch of Tubulin and Microtubule
974   Assembly: A Polymerization-Driven Structural Change. *Biochemistry* **45**:5933–5938.
975   doi:10.1021/bi060334m

976 Buscaglia G, Aiken J, Hoff KJ, Northington KR, Bates EA. 2020a. Tuba1a is uniquely important for
977   axon guidance through midline commissural structures. *bioRxiv* 2020.05.05.079376.
978   doi:10.1101/2020.05.05.079376

979 Buscaglia G, Northington KR, Moore JK, Bates EA. 2020b. Reduced TUBA1A tubulin causes
980   defects in trafficking and impaired adult motor behavior. *eNeuro* ENEURO.0045-
981   20.2020. doi:10.1523/ENEURO.0045-20.2020

982 Chakraborti S, Natarajan K, Curiel J, Janke C, Liu J. 2016. The emerging role of the tubulin code:
983   From the tubulin molecule to neuronal function and disease. *Cytoskeleton* **73**:521–550.
984   doi:10.1002/cm.21290

985 Chesta ME, Carbajal A, Arce CA, Bisig CG. 2014. Serum-induced neurite retraction in CAD
986   cells – involvement of an ATP-actin retractile system and the lack of microtubule-
987   associated proteins. *The FEBS Journal* **281**:4767–4778. doi:10.1111/febs.12967

988 Chrétien D, Fuller SD, Karsenti E. 1995. Structure of growing microtubule ends: two-dimensional
989   sheets close into tubes at variable rates. *J Cell Biol* **129**:1311–1328.
990   doi:10.1083/jcb.129.5.1311

991 Cooper JA. 2014. Molecules and mechanisms that regulate multipolar migration in the
992   intermediate zone. *Front Cell Neurosci* **8**:386–386. doi:10.3389/fncel.2014.00386

993 Das A, Dickinson DJ, Wood CC, Goldstein B, Slep KC. 2015. Crescerin uses a TOG domain array to
994   regulate microtubules in the primary cilium. *Mol Biol Cell* **26**:4248–4264.
995   doi:10.1091/mbc.E15-08-0603

996 Dehmelt L, Nalbant P, Steffen W, Halpain S. 2006. A microtubule-based, dynein-dependent
997   force induces local cell protrusions: Implications for neurite initiation. *Brain Cell Biology*
998   **35**:39–56. doi:10.1007/s11068-006-9001-0

999 Dent EW, Baas PW. 2014. Microtubules in neurons as information carriers. *J Neurochem*
1000   **129**:235–239. doi:10.1111/jnc.12621

Dent EW, Gupton SL, Gertler FB. 2011. The growth cone cytoskeleton in axon outgrowth and guidance. *Cold Spring Harb Perspect Biol* **3**:a001800. doi:10.1101/cshperspect.a001800

Dent EW, Kalil K. 2001. Axon branching requires interactions between dynamic microtubules and actin filaments. *J Neurosci* **21**:9757–9769. doi:10.1523/JNEUROSCI.21-24-09757.2001

Dotti CG, Sullivan CA, Banker GA. 1988. The establishment of polarity by hippocampal neurons in culture. *J Neurosci* **8**:1454–1468. doi:10.1523/JNEUROSCI.08-04-01454.1988

Fallet-Bianco C, Laquerrière A, Poirier K, Razavi F, Guimiot F, Dias P, Loeuillet L, Lascelles K, Beldjord C, Carion N, Toussaint A, Revencu N, Addor M-C, Lhermitte B, Gonzales M, Martinovich J, Bessieres B, Marcy-Bonnière M, Jossic F, Marcorelles P, Loget P, Chelly J, Bahi-Buisson N. 2014. Mutations in tubulin genes are frequent causes of various foetal malformations of cortical development including microlissencephaly. *Acta Neuropathol Commun* **2**:69–69. doi:10.1186/2051-5960-2-69

Falnikar A, Tole S, Liu M, Liu JS, Baas PW. 2013. Polarity in migrating neurons is related to a mechanism analogous to cytokinesis. *Curr Biol* **23**:1215–1220. doi:10.1016/j.cub.2013.05.027

Farmer V, Arpağ G, Hall SL, Zanic M. 2021. XMAP215 promotes microtubule catastrophe by disrupting the growing microtubule end. *Journal of Cell Biology* **220**. doi:10.1083/jcb.202012144

Fees CP, Aiken J, O'Toole ET, Giddings TH Jr, Moore JK. 2016. The negatively charged carboxy-terminal tail of β-tubulin promotes proper chromosome segregation. *Mol Biol Cell* **27**:1786–1796. doi:10.1091/mbc.E15-05-0300

Fees CP, Moore JK. 2018. Regulation of microtubule dynamic instability by the carboxy-terminal tail of β-tubulin. *Life Sci Alliance* **1**:e201800054. doi:10.26508/lsa.201800054

Fourniol FJ, Sindelar CV, Amigues B, Clare DK, Thomas G, Perderiset M, Francis F, Houdusse A, Moores CA. 2010. Template-free 13-protofilament microtubule-MAP assembly visualized at 8 A resolution. *J Cell Biol* **191**:463–470. doi:10.1083/jcb.201007081

Gartz Hanson M, Aiken J, Sietsema DV, Sept D, Bates EA, Niswander L, Moore JK. 2016. Novel α-tubulin mutation disrupts neural development and tubulin proteostasis. *Dev Biol* **409**:406–419. doi:10.1016/j.ydbio.2015.11.022

Geyer EA, Burns A, Lalonde BA, Ye X, Piedra F-A, Huffaker TC, Rice LM. 2015. A mutation uncouples the tubulin conformational and GTPase cycles, revealing allosteric control of microtubule dynamics. *eLife* **4**:e10113. doi:10.7554/eLife.10113

Geyer EA, Miller MP, Brautigam CA, Biggins S, Rice LM. 2018. Design principles of a microtubule polymerase. *Elife* **7**:e34574. doi:10.7554/eLife.34574

Gloster A, El-Bizri H, Bamji SX, Rogers D, Miller FD. 1999. Early induction of Tα1 α-tubulin transcription in neurons of the developing nervous system. *Journal of Comparative Neurology* **405**:45–60. doi:10.1002/(SICI)1096-9861(19990301)405:1<45::AID-CNE4>3.0.CO;2-M

Gloster A, Wu W, Speelman A, Weiss S, Causing C, Pozniak C, Reynolds B, Chang E, Toma JG, Miller FD. 1994. The T alpha 1 alpha-tubulin promoter specifies gene expression as a function of neuronal growth and regeneration in transgenic mice. *J Neurosci* **14**:7319–7330. doi:10.1523/JNEUROSCI.14-12-07319.1994

1044 Goodson HV, Jonasson EM. 2018. Microtubules and Microtubule-Associated Proteins. *Cold*
1045   *Spring Harb Perspect Biol* **10**:a022608. doi:10.1101/cshperspect.a022608

1046 Hahn I, Voelzmann A, Parkin J, Fülle JB, Slater PG, Lowery LA, Sanchez-Soriano N, Prokop A.
1047   2021. Tau, XMAP215/Msps and Eb1 co-operate interdependently to regulate
1048   microtubule polymerisation and bundle formation in axons. *PLOS Genetics* **17**:e1009647.
1049   doi:10.1371/journal.pgen.1009647

1050 Hand R, Bortone D, Mattar P, Nguyen L, Heng JI-T, Guerrier S, Boutt E, Peters E, Barnes AP,
1051   Parras C, Schuurmans C, Guillemot F, Polleux F. 2005. Phosphorylation of Neurogenin2
1052   Specifies the Migration Properties and the Dendritic Morphology of Pyramidal Neurons
1053   in the Neocortex. *Neuron* **48**:45–62. doi:10.1016/j.neuron.2005.08.032

1054 He Y, Yu W, Baas PW. 2002. Microtubule Reconfiguration during Axonal Retraction Induced by
1055   Nitric Oxide. *J Neurosci* **22**:5982. doi:10.1523/JNEUROSCI.22-14-05982.2002

1056 Hebebrand M, Hüffmeier U, Trollmann R, Hehr U, Uebe S, Ekici AB, Kraus C, Krumbiegel M, Reis
1057   A, Thiel CT, Popp B. 2019. The mutational and phenotypic spectrum of TUBA1A-
1058   associated tubulinopathy. *Orphanet J Rare Dis* **14**:38–38. doi:10.1186/s13023-019-1020-
1059   x

1060 Horio T, Hotani H. 1986. Visualization of the dynamic instability of individual microtubules by
1061   dark-field microscopy. *Nature* **321**:605–607. doi:10.1038/321605a0

1062 Hussmann F, Drummond DR, Peet DR, Martin DS, Cross RA. 2016. Alp7/TACC-Alp14/TOG
1063   generates long-lived, fast-growing MTs by an unconventional mechanism. *Sci Rep*
1064   **6**:20653–20653. doi:10.1038/srep20653

1065 Jánosi IM, Chrétien D, Flyvbjerg H. 1998. Modeling elastic properties of microtubule tips and
1066   walls. *European Biophysics Journal* **27**:501–513. doi:10.1007/s002490050160

1067 Jordan MA, Toso RJ, Thrower D, Wilson L. 1993. Mechanism of mitotic block and inhibition of
1068   cell proliferation by taxol at low concentrations. *Proc Natl Acad Sci U S A* **90**:9552–9556.
1069   doi:10.1073/pnas.90.20.9552

1070 Kapitein LC, Hoogenraad CC. 2015. Building the Neuronal Microtubule Cytoskeleton. *Neuron*
1071   **87**:492–506. doi:10.1016/j.neuron.2015.05.046

1072 Keays DA, Tian G, Poirier K, Huang G-J, Siebold C, Cleak J, Oliver PL, Fray M, Harvey RJ, Molnár Z,
1073   Piñon MC, Dear N, Valdar W, Brown SDM, Davies KE, Rawlins JNP, Cowan NJ, Nolan P,
1074   Chelly J, Flint J. 2007. Mutations in alpha-tubulin cause abnormal neuronal migration in
1075   mice and lissencephaly in humans. *Cell* **128**:45–57. doi:10.1016/j.cell.2006.12.017

1076 Kosco KA, Pearson CG, Maddox PS, Wang PJ, Adams IR, Salmon ED, Bloom K, Huffaker TC. 2001.
1077   Control of microtubule dynamics by Stu2p is essential for spindle orientation and
1078   metaphase chromosome alignment in yeast. *Mol Biol Cell* **12**:2870–2880.
1079   doi:10.1091/mbc.12.9.2870

1080 Lasser M, Tiber J, Lowery LA. 2018. The Role of the Microtubule Cytoskeleton in
1081   Neurodevelopmental Disorders. *Frontiers in Cellular Neuroscience* **12**:165.
1082   doi:10.3389/fncel.2018.00165

1083 Lee MJ, Gergely F, Jeffers K, Peak-Chew SY, Raff JW. 2001. Msps/XMAP215 interacts with the
1084   centrosomal protein D-TACC to regulate microtubule behaviour. *Nature Cell Biology*
1085   **3**:643–649. doi:10.1038/35083033

1086 Lin S, Liu M, Mozgova OI, Yu W, Baas PW. 2012. Mitotic motors coregulate microtubule
1087   patterns in axons and dendrites. *J Neurosci* **32**:14033–14049.
1088   doi:10.1523/JNEUROSCI.3070-12.2012

1089 Löwe J, Li H, Downing KH, Nogales E. 2001. Refined structure of αβ-tubulin at 3.5 Å
1090   resolution11Edited by I. A. Wilson. *Journal of Molecular Biology* **313**:1045–1057.
1091   doi:10.1006/jmbi.2001.5077

1092 Lowery LA, Stout A, Faris AE, Ding L, Baird MA, Davidson MW, Danuser G, Van Vactor D. 2013.
1093   Growth cone-specific functions of XMAP215 in restricting microtubule dynamics and
1094   promoting axonal outgrowth. *Neural Dev* **8**:22–22. doi:10.1186/1749-8104-8-22

1095 Lu W, Fox P, Lakonishok M, Davidson MW, Gelfand VI. 2013. Initial Neurite Outgrowth in
1096   Drosophila Neurons Is Driven by Kinesin-Powered Microtubule Sliding. *Current Biology*
1097   **23**:1018–1023. doi:10.1016/j.cub.2013.04.050

1098 Ludueña RF, Banerjee A. 2008. The Tubulin Superfamily In: Fojo T, editor. The Role of
1099   Microtubules in Cell Biology, Neurobiology, and Oncology. Totowa, NJ: Humana Press.
1100   pp. 177–191. doi:10.1007/978-1-59745-336-3_7

1101 MAHAMDEH M, SIMMERT S, LUCHNIAK A, SCHÄFFER E, HOWARD J. 2018. Label-free high-speed
1102   wide-field imaging of single microtubules using interference reflection microscopy.
1103   *Journal of Microscopy* **272**:60–66. doi:10.1111/jmi.12744

1104 Mandelkow EM, Mandelkow E, Milligan RA. 1991. Microtubule dynamics and microtubule caps:
1105   a time-resolved cryo-electron microscopy study. *Journal of Cell Biology* **114**:977–991.
1106   doi:10.1083/jcb.114.5.977

1107 Manka SW, Moores CA. 2020. Pseudo-repeats in doublecortin make distinct mechanistic
1108   contributions to microtubule regulation. *EMBO Rep* **21**:e51534–e51534.
1109   doi:10.15252/embr.202051534

1110 Manka SW, Moores CA. 2018. Microtubule structure by cryo-EM: snapshots of dynamic
1111   instability. *Essays Biochem* **62**:737–751. doi:10.1042/EBC20180031

1112 Matsuo Y, Maurer SP, Yukawa M, Zakian S, Singleton MR, Surrey T, Toda T. 2016. An
1113   unconventional interaction between Dis1/TOG and Mal3/EB1 in fission yeast promotes
1114   the fidelity of chromosome segregation. *J Cell Sci* **129**:4592–4606.
1115   doi:10.1242/jcs.197533

1116 Meijering E, Jacob M, Sarria J-CF, Steiner P, Hirling H, Unser M. 2004. Design and validation of a
1117   tool for neurite tracing and analysis in fluorescence microscopy images. *Cytometry Part
1118   A* **58A**:167–176. doi:10.1002/cyto.a.20022

1119 Miller RK. 2004. Monitoring Spindle Assembly and Disassembly in Yeast by Indirect
1120   Immunofluorescence In: Lieberman HB, editor. Cell Cycle Checkpoint Control Protocols.
1121   Totowa, NJ: Humana Press. pp. 341–352. doi:10.1385/1-59259-646-0:341

1122 Minoura I, Hachikubo Y, Yamakita Y, Takazaki H, Ayukawa R, Uchimura S, Muto E. 2013.
1123   Overexpression, purification, and functional analysis of recombinant human tubulin
1124   dimer. *FEBS Letters* **587**:3450–3455. doi:10.1016/j.febslet.2013.08.032

1125 Mitchison T, Kirschner M. 1984. Dynamic instability of microtubule growth. *Nature* **312**:237–
1126   242. doi:10.1038/312237a0

1127 Moores CA, Perderiset M, Kappeler C, Kain S, Drummond D, Perkins SJ, Chelly J, Cross R,
1128   Houdusse A, Francis F. 2006. Distinct roles of doublecortin modulating the microtubule
1129   cytoskeleton. *EMBO J* **25**:4448–4457. doi:10.1038/sj.emboj.7601335

1130 Nadarajah B, Brunstrom JE, Grutzendler J, Wong ROL, Pearlman AL. 2001. Two modes of radial
1131   migration in early development of the cerebral cortex. *Nature Neuroscience* **4**:143–150.
1132   doi:10.1038/83967

1133 Nawrotek A, Knossow M, Gigant B. 2011. The Determinants That Govern Microtubule Assembly
1134   from the Atomic Structure of GTP-Tubulin. *Journal of Molecular Biology* **412**:35–42.
1135   doi:10.1016/j.jmb.2011.07.029

1136 Noctor SC, Martínez-Cerdeño V, Ivic L, Kriegstein AR. 2004. Cortical neurons arise in symmetric
1137   and asymmetric division zones and migrate through specific phases. *Nature*
1138   *Neuroscience* **7**:136–144. doi:10.1038/nn1172

1139 Nogales E, Wang H-W. 2006. Structural mechanisms underlying nucleotide-dependent self-
1140   assembly of tubulin and its relatives. *Current Opinion in Structural Biology* **16**:221–229.
1141   doi:10.1016/j.sbi.2006.03.005

1142 Ohshima T, Hirasawa M, Tabata H, Mutoh T, Adachi T, Suzuki H, Saruta K, Iwasato T, Itohara S,
1143   Hashimoto M, Nakajima K, Ogawa M, Kulkarni AB, Mikoshiba K. 2007. Cdk5 is required
1144   for multipolar-to-bipolar transition during radial neuronal migration and proper
1145   dendrite development of pyramidal neurons in the cerebral cortex. *Development*
1146   **134**:2273–2282. doi:10.1242/dev.02854

1147 Podolski M, Mahamdeh M, Howard J. 2014. Stu2, the budding yeast XMAP215/Dis1 homolog,
1148   promotes assembly of yeast microtubules by increasing growth rate and decreasing
1149   catastrophe frequency. *J Biol Chem* **289**:28087–28093. doi:10.1074/jbc.M114.584300

1150 Ravelli RBG, Gigant B, Curmi PA, Jourdain I, Lachkar S, Sobel A, Knossow M. 2004. Insight into
1151   tubulin regulation from a complex with colchicine and a stathmin-like domain. *Nature*
1152   **428**:198–202. doi:10.1038/nature02393

1153 Reusch S, Biswas A, Hirst WG, Reber S. 2020. Affinity Purification of Label-free Tubulins from
1154   Xenopus Egg Extracts. *STAR Protoc* **1**:100151–100151. doi:10.1016/j.xpro.2020.100151

1155 Rice LM, Montabana EA, Agard DA. 2008. The lattice as allosteric effector: structural studies of
1156   alphabeta- and gamma-tubulin clarify the role of GTP in microtubule assembly. *Proc Natl*
1157   *Acad Sci U S A* **105**:5378–5383. doi:10.1073/pnas.0801155105

1158 Roostalu J, Thomas C, Cade NI, Kunzelmann S, Taylor IA, Surrey T. 2020. The speed of GTP
1159   hydrolysis determines GTP cap size and controls microtubule stability. *eLife* **9**:e51992.
1160   doi:10.7554/eLife.51992

1161 Sainath R, Gallo G. 2015. Cytoskeletal and signaling mechanisms of neurite formation. *Cell and*
1162   *Tissue Research* **359**:267–278. doi:10.1007/s00441-014-1955-0

1163 Slater PG, Cammarata GM, Samuelson AG, Magee A, Hu Y, Lowery LA. 2019. XMAP215
1164   promotes microtubule-F-actin interactions to regulate growth cone microtubules during
1165   axon guidance in Xenopus laevis. *J Cell Sci* **132**:jcs224311. doi:10.1242/jcs.224311

1166 Slep KC, Vale RD. 2007. Structural basis of microtubule plus end tracking by XMAP215, CLIP-170,
1167   and EB1. *Mol Cell* **27**:976–991. doi:10.1016/j.molcel.2007.07.023

1168 Srivastava AK, Schwartz CE. 2014. Intellectual disability and autism spectrum disorders: Causal
1169   genes and molecular mechanisms. *Neuroscience & Biobehavioral Reviews* **46**:161–174.
1170   doi:10.1016/j.neubiorev.2014.02.015

1171 Studier FW. 2005. Protein production by auto-induction in high-density shaking cultures.
1172   *Protein Expression and Purification* **41**:207–234. doi:10.1016/j.pep.2005.01.016

1173 Tabata H, Nakajima K. 2003. Multipolar Migration: The Third Mode of Radial Neuronal
1174   Migration in the Developing Cerebral Cortex. *J Neurosci* **23**:9996.
1175   doi:10.1523/JNEUROSCI.23-31-09996.2003

1176 Tilney LG, Porter KR. 1967. Studies on the microtubules in heliozoa. II. The effect of low
1177   temperature on these structures in the formation and maintenance of the axopodia. *J*
1178   *Cell Biol* **34**:327–343. doi:10.1083/jcb.34.1.327

1179 van der Vaart B, Manatschal C, Grigoriev I, Olieric V, Gouveia SM, Bjelic S, Demmers J, Vorobjev
1180   I, Hoogenraad CC, Steinmetz MO, Akhmanova A. 2011. SLAIN2 links microtubule plus
1181   end-tracking proteins and controls microtubule growth in interphase. *J Cell Biol*
1182   **193**:1083–1099. doi:10.1083/jcb.201012179

1183 Vasquez RJ, Gard DL, Cassimeris L. 1994. XMAP from Xenopus eggs promotes rapid plus end
1184   assembly of microtubules and rapid microtubule polymer turnover. *J Cell Biol* **127**:985–
1185   993. doi:10.1083/jcb.127.4.985

1186 Walker RA, O'Brien ET, Pryer NK, Soboeiro MF, Voter WA, Erickson HP, Salmon ED. 1988.
1187   Dynamic instability of individual microtubules analyzed by video light microscopy: rate
1188   constants and transition frequencies. *J Cell Biol* **107**:1437–1448.
1189   doi:10.1083/jcb.107.4.1437

1190 Weber K, Pollack R, Bibring T. 1975. Antibody against tuberlin: the specific visualization of
1191   cytoplasmic microtubules in tissue culture cells. *Proc Natl Acad Sci U S A* **72**:459–463.
1192   doi:10.1073/pnas.72.2.459

1193 Westermann S, Weber K. 2003. Post-translational modifications regulate microtubule function.
1194   *Nature Reviews Molecular Cell Biology* **4**:938–948. doi:10.1038/nrm1260

1195 Widlund PO, Podolski M, Reber S, Alper J, Storch M, Hyman AA, Howard J, Drechsel DN. 2012.
1196   One-step purification of assembly-competent tubulin from diverse eukaryotic sources.
1197   *Mol Biol Cell* **23**:4393–4401. doi:10.1091/mbc.E12-06-0444

1198 Winding M, Kelliher MT, Lu W, Wildonger J, Gelfand VI. 2016. Role of kinesin-1–based
1199   microtubule sliding in Drosophila nervous system development. *Proc Natl*
1200   *Acad Sci USA* **113**:E4985. doi:10.1073/pnas.1522416113

1201 Witte H, Neukirchen D, Bradke F. 2008. Microtubule stabilization specifies initial neuronal
1202   polarization. *J Cell Biol* **180**:619–632. doi:10.1083/jcb.200707042

1203 Zanic M, Widlund PO, Hyman AA, Howard J. 2013. Synergy between XMAP215 and EB1
1204   increases microtubule growth rates to physiological levels. *Nature Cell Biology* **15**:688–
1205   693. doi:10.1038/ncb2744

1206 Zheng Y, Wong ML, Alberts B, Mitchison T. 1995. Nucleation of microtubule assembly by a γ-
1207   tubulin-containing ring complex. *Nature* **378**:578–583. doi:10.1038/378578a0
1208